Monthly Notices of the ROYAL ASTRONOMICAL SOCIETY

MNRAS **546,** 1–18 (2026)
Advance Access publication 2026 January 14

https://doi.org/10.1093/mnras/stag087

Mass estimates of the young TOI-451 transiting planets: multidimensional Gaussian Process on stellar spectroscopic and photometric signals

Oscar Barragán [1,2★] Manuel Mallorquín,[3,4] Jorge Fernández-Fernández [2,5] Faith Hawthorn [2,5] Alix V. Freckelton [6] Marina Lafarga [2,5] Michael Cretignier [1] Yoshi N. E. Eschen [2,5] Samuel Gill,[2,5] Víctor J. S. Béjar,[3,4] Nicolas Lodieu,[3,4] Haochuan Yu [1] Thomas G. Wilson [2,5] David Anderson,[7] Ioannis Apergis [2,5] Matthew Battley [8,9] Edward M. Bryant [2] Pía Cortés-Zuleta,[10] Edward Gillen [8] James S. Jenkins,[11,12] Baptiste Klein [1] James McCormac,[2,5] Annabella Meech [13] Erik Meier-Valdés,[1] Maximiliano Moyano,[7] Annelies Mortier [6] Felipe Murgas,[3,4] Louise D. Nielsen [14] Suman Saha [13,14] José I. Vines [7] Richard West [2,5] Peter J. Wheatley [2,5] and Suzanne Aigrain[1]

Affiliations are listed at the end of the paper

Accepted 2026 January 12. Received 2026 January 6; in original form 2025 May 7

ABSTRACT

The young TOI-451 planetary system, aged 125 Myr, provides a unique opportunity to test theories of planetary internal structures and atmospheric mass-loss through examination of its three transiting planets. We present an exhaustive photometric and spectroscopic follow-up to determine the orbital and physical properties of the system. We perform multidimensional Gaussian Process regression with the code `pyaneti` on spectroscopic time-series and NGTS/LCO light curves to disentangle the stellar and planetary signal in ESPRESSO radial velocities. We show how contemporaneous photometry serves as an activity indicator to inform RV modelling within a multidimensional Gaussian Processes framework. We argue that this can be exploited when spectroscopic observations are adversely affected by low signal-to-noise and/or poor sampling. We estimate the Doppler semi-amplitudes of $k_b = 2.6^{+1.1}_{-1.2}\,\mathrm{m\,s^{-1}}$, $k_c = 1.2^{+1.0}_{-0.8}\,\mathrm{m\,s^{-1}}$, and $k_d = 2.7 \pm 1.2\,\mathrm{m\,s^{-1}}$. This translates in 2σ mass estimates for TOI-451 b and d of $M_b = 4.7^{+2.1}_{-2.2}\,\mathrm{M_\oplus}$ and $M_d = 10.2^{+4.6}_{-4.5}\,\mathrm{M_\oplus}$; as well as a mass upper limit for TOI-451 c of $M_c < 11.5\,M_\oplus$. The derived planetary properties suggest that planets c and d contain significant hydrogen-rich envelopes. The inferred parameters of TOI-451 b are consistent with either a rocky world that still retains a small hydrogen envelope or a water world. These insights make the TOI-451 system an ideal laboratory for future follow-up studies aimed at measuring atmospheric compositions, detecting atmospheric mass-loss signatures, and further exploring planetary formation and evolution processes.

Key words: techniques: photometric – techniques: radial velocities – planets and satellites: individual: TOI-451 – stars: activity.

1 INTRODUCTION

One of the current challenges of exoplanetary science is the characterization of young exoplanets (< 1 Gyr) due to their host star's high activity levels. Exoplanets in nearby young stellar associations are especially valuable for studying early planetary evolution, as they are subject to rapid processes such as orbital migration, tidal circularization, atmospheric escape, and thermal cooling – all of which significantly impact their physical and orbital characteristics. The well-constrained ages of these systems allow for robust estimates of the time-scales over which these mechanisms operate (e.g. J. E. Owen & Y. Wu 2013). Planets in these environments also provide critical insights to understand the origin of the bimodal radius distribution (the 'radius valley') observed among close-in super-Earths and sub-Neptunes (B. J. Fulton et al. 2017). They serve as a crucial test for distinguishing between the photoevaporation-driven mass-loss scenario (J. E. Owen & Y. Wu 2017) and the core-powered mass-loss hypothesis (S. Ginzburg, H. E. Schlichting & R. Sari 2016), which predict atmospheric evolution on markedly different time-scales ∼100 Myr and ∼1 Gyr, respectively.

Radial velocity (RV) follow-up of transiting exoplanets is a standard approach that allows us to characterize, at first order, planetary nature. However, this is not straightforward for young star systems. Young stars are characterized by intense magnetic activity, which manifests in various phenomena on their surfaces

★ E-mail: oscar.barragan@physics.ox.ac.uk, oscar.barragan@warwick.ac.uk

(e.g. A. F. Lanza 2006). A prominent feature of this activity is the presence of starspots – regions with distinct temperature and brightness – on the stellar surface (e.g. M. Huerta et al. 2008). These starspots differ in size and distribution, and as the star rotates, they cause significant photometric fluctuations, often much larger than the signals produced by transiting exoplanets (e.g. B. M. Morris 2020). Surface activity also impacts the stellar spectra used in RV measurements (e.g. S. H. Saar & R. A. Donahue 1997). Variations in the spectral line profiles, such as changes in their shape, depth, or symmetry, as well as the appearance of spurious emission or absorption features, can distort the observed spectrum. These alterations introduce apparent RV variations that do not correspond to actual motion, complicating the detection of planetary signals. In the case of young stars, such activity-driven RV signals can span from several tens to several hundreds of metres per second (e.g. O. Barragán et al. 2019b, 2022b; A. Suárez Mascareño et al. 2021; N. Zicher et al. 2022).

Multidimensional Gaussian Process (multi-GP; V. Rajpaul et al. 2015) regression is nowadays a standard to detect the RV signals of planets orbiting young and/or active stars (A. W. Mayo et al. 2019; O. Barragán et al. 2019b, 2022b; D. Nardiello et al. 2022; N. Zicher et al. 2022; R. Luque et al. 2023). S. Aigrain, F. Pont & S. Zucker (2012) proposed the FF' framework to connect the activity-induced photometric flux and RV variations, taking into account its different dependencies on the evolution of the active regions on the stellar surface. The multi-GP framework of V. Rajpaul et al. (2015) appeared as a generalization of the FF' framework to allow the use of spectral activity indicators instead of photometry. This multi-GP approach is also a solution to the lack of contemporaneous photometry to RV observations by exploiting the simultaneity of the activity indicators that are extracted from the same spectra that the RVs are computed (V. Rajpaul et al. 2015).[1] However, recent studies have shown that the multi-GP framework fails to model the stellar signal if the spectroscopic observations do not sample well the stellar signal time-scales (e.g. M. Fridlund et al. 2024; O. Barragán et al. 2024b).

Recent studies have used contemporaneous photometry to sample the stellar signal with better cadence to help disentangle the stellar and planetary signals from the RVs (A. Suárez Mascareño et al. 2023; J. I. González Hernández et al. 2024; C. Beard et al. 2025). These studies use a sequential modelling approach, where a onedimensional (1D) GP regression is performed on the photometry, and the posteriors of the GP kernel hyperparameters are then used as priors when modelling the RV time-series (R. D. Haywood et al. 2014). In this approach, different functions are used to model the stellar signal in photometry and RVs, though they have common covariance properties. Thus, this fails to exploit the connection between photometry and RVs fully. Furthermore, 1D GP regressions on photometry and RVs yield different hyperparameters (see B. A. Nicholson & S. Aigrain 2022; O. Barragán et al. 2022a), so training a 1D GP on photometry before applying it to RVs does not necessarily improve the performance. To our knowledge, a tailored multi-GP regression including contemporaneous photometry and RV observations is still to be tested. We explore this scenario in this manuscript by modelling contemporaneous spectroscopic and photometric time-series of the young star TOI-451.

[1]In this work we refer to events occurring at the exact same time as simultaneous, while contemporaneous denotes events within the same period, but not necessarily at the same instant.

Using observations collected by NASA's Transiting Exoplanet Survey Satellite (*TESS*; G. R. Ricker et al. 2015), E. R. Newton et al. (2021, hereafter N21) identified a planetary system consisting of three small transiting planets orbiting the star TOI-451, a G star belonging to of the young (125 Myr) Pisces–Eridanus stellar stream. The transiting planets, TOI-451 b, c, and d, have periods of 1.86, 9.2, and 16.4 d and radii of 1.9, 3.1, and 4.1 $R_\oplus$, respectively. Given that the host star is relatively bright ($V = 10.94$), the target was identified as well-suited for additional follow-up observations, such as RV measurements to determine planetary masses, as well as transmission spectroscopy to probe the planets' atmospheres (N. E. Batalha et al. 2019). Further detailed characterization of a system like TOI-451 can provide critical constraints for models of planetary formation and early evolution. We now present the results of an intense ground-based follow-up campaign of spectroscopic and photometric observations of this system.

This paper is structured as follows: The photometric and spectroscopic data of TOI-451 are detailed in Section 2. The analytical methods applied to these data are outlined in Section 3. A discussion of the findings is provided in Section 4, and the paper concludes with a summary of the key outcomes in Section 5. This manuscript is part of a series of papers under the project *GPRV: Overcoming stellar activity in RV planet searches* funded by the European Research Council (ERC, P.I. S. Aigrain).

2 TOI-451 DATA

2.1 *TESS* data

TESS initially observed TOI-451 (TIC 257605131) during its first cycle, covering sectors 4 and 5 (from 2018-Oct-18 to 2018-Dec-11). These observations, together with supplementary ground and space-based data, enabled N21 to discover and confirm three transiting planets orbiting TOI-451. These planets, named TOI-451 b, c and d, have periods of 1.9, 9.2 and 16.4 d, with corresponding radii of 1.91 ± 0.12, 3.1 ± 0.13, and 4.07 ± 0.15 $R_\oplus$, respectively. For a detailed description of the discovery and validation of this planetary system, see N21.

Two years later, *TESS* returned to observe TOI-451 during its extended mission, as part of Cycle 3 in sector 31 (from 2020-Oct-21 to 2020-Nov-19). O. Barragán et al. (2021) and A. Kokori et al. (2023) used all available *TESS* data to refine the planetary ephemerides and radii. These two manuscripts are the ones that present the last analyses performed on transits of TOI-451. For this paper, we use the same *TESS* data as described and processed in O. Barragán et al. (2021).

TOI-451 will be re-observed by *TESS* in Sectors 106 and 107 (2026 July and August), according to the *TESS*-point Web Tool.[2] It is also worth noting that TOI-451 is planned to be observed by the *PLATO* mission (H. Rauer et al. 2024) in its first two years of observations (see Y. N. E. Eschen et al. 2024, and further discussion in Section 4.3).

2.2 NGTS photometry

The Next Generation Transit Survey (NGTS; P. J. Wheatley et al. 2018) is a photometric facility consisting of twelve independently

[2]https://heasarc.gsfc.nasa.gov/wsgi-scripts/TESS/TESS-point_Web_Tool/TESS-point_Web_Tool/wtv_v2.0.py

steerable robotic telescopes situated at ESO's Paranal Observatory in Chile. Each NGTS telescope has a 20 cm diameter aperture and observes a very wide field-of-view (2.8 × 2.8 degrees) using a custom filter (520–890 nm; P. J. Wheatley et al. 2018). Each telescope has Andor iKon L cameras with deep-depleted, red-sensitive, and back-sided illuminated CCDs. The precision of NGTS observations is scintillation limited for bright stars ($G < 11$ mag; S. M. O'Brien et al. 2022) and by using multiple NGTS telescopes to simultaneously observe the same star, we can achieve photometric precisions on the order of 100 ppm-per-30 min (E. M. Bryant et al. 2020).

We observed TOI-451 with NGTS with two objectives. First, to obtain contemporaneous photometry to the ESPRESSO data to monitor the stellar variability of the host star. For these observations, TOI-451 was observed for 30 min on every night that the telescope opened between 2023-08-18 to 2024-02-09, using the same telescope observing at a similar airmass and with precise auto-guiding to ensure consistent photometry night-to-night. Such monitoring observations have been previously performed by NGTS to monitor stellar variability in support of spectroscopic observations (e.g. E.-M. Ahrer et al. 2023). Because we are interested in the signal evolution on time-scales of days, we binned the data to one point per night. The NGTS monitoring photometry is shown and discussed in Sections 3.3 and 3.4. NGTS time series can be accesed in the online version of Table 2.

The second objective was to obtain transits of planets c and d to refine the ephemerides and planet radii. We observed two transits of TOI-451 c, observing the transit egress on the night of 2024-10-15 using six NGTS telescopes and a full transit on the night of 2024-10-24 using five NGTS telescopes. We observed an egress of TOI-451 d using five NGTS telescopes on 2024-12-13. The three NGTS observations were all performed using an exposure time of 10 s, resulting in a total of 10894, 9710, and 10 320 images for the three nights of observations, respectively. The NGTS images were reduced and the photometry was extracted using a custom version of the standard NGTS pipeline, which is described in P. J. Wheatley et al. (2018). This custom version is designed to obtain high-precision photometry for a specific target star. We flattened the transits by fitting a second-order polynomial to the out-of-transit data using `citlalicue` (O. Barragán et al. 2022a). The NGTS transit photometry is shown and discussed in Sections 3.2 and 3.5. Orange colour will be used in this paper for all the NGTS-related data/models.

2.3 LCO photometry

We also monitored TOI-451 during 112 d between 2023 November 14 and 2024 March 5, using the two 40 cm telescopes of Las Cumbres Observatory Global Telescope (T. M. Brown et al. 2013) at Las Campanas Observatory. We observed the target in the V band and obtained about 78 useful epochs (about 2 epochs per 3 d), each of them with typically 10 individual exposures of 60s per epoch. The 40 cm telescopes have a 3k × 2k SBIG CCD camera with a pixel scale of 0.571 arcsec providing a field of view of 29.2 × 19.5 arcmin. Weather conditions were clear, and the average seeing varies from 3 to 6 arcsec. Raw data was processed using the `BANZAI` pipeline (C. McCully et al. 2018), which includes bad pixel, bias, dark, and flat field corrections for each night. We performed aperture differential photometry using AstroImageJ (K. A. Collins et al. 2017), adopting an aperture of 10 pixels (5.7 arcsec). The LCO photometry is shown and analysed in Sections 3.3 and 3.4. LCO time series can be acceded in the online version of Table 2. Purple colour will be used in this paper for all the LCO-related data/models.

2.4 Spectroscopic observations

We acquired 134 ESPRESSO spectra of TOI-451 between 2023 October and 2024 March. ESPRESSO (F. Pepe et al. 2021) is a high-resolution spectrograph mounted on the 8.2 m Very Large Telescope (VLT; Paranal, Chile). The observations were taken as part of the ESO P112 programmes 112.261J.001 (P.I. Barragán) and 112.25HY.001 (P.I. Mallorquín). Each observation has an integration time of 900 s, a median resolving power of 140 000, and a wavelength range of 380–788 nm. Observations were taken in high-resolution mode. Given the complex stellar activity in TOI-451, we reduced the spectra with different frameworks to cross validate the extracted RVs and activity indicators. Below, we describe the different methods used to reduce the spectra.

We note that 26 archival HARPS observations of TOI-451 were taken in 2019 (under the programme: 0103.C-0759(A) by P.I. Benatti). These observations show peak-to-peak variations of the order of 100 m s^{-1}, indicating activity-induced signals. However, as these observations were taken several years before the ESPRESSO observations, the stellar signal has evolved, and these data are not helpful to constrain the stellar signal in the ESPRESSO time-series (O. Barragán et al. 2021). Furthermore, they do not have sufficient time-sampling or signal-to-noise to constrain the local shape of the stellar signal by themselves. Therefore, we decided not to include them in our analysis.

2.4.1 DRS

We reduced the raw ESPRESSO data with the official Data Reduction Software[3] (DRS) version 3.0.0. The DRS performs standard echelle spectrum reduction, including bias and dark subtraction, optimal order extraction, bad pixel correction, flat-fielding, deblazing, wavelength calibration, and order merging (see F. Pepe et al. 2021, for details). We also used the DRS to compute cross-correlation functions (CCFs) with the default ESPRESSO G9 mask. For each observation, the CCFs are computed on an order-by-order basis, and a final CCF is obtained by coadding the individual-order CCFs. A Gaussian function is then fitted to each coadded CCF, and the RV of each observation is obtained from the centroid of the best-fitting Gaussian. The DRS provides activity indicators extracted from the CCF profile: the full width at half-maximum (FWHM), also obtained from the Gaussian fit, and the bisector span (BIS), which measures the asymmetry of the CCF by computing the difference in average RV between the top and the bottom parts of the CCF profile, as described in D. Queloz et al. (2001). The DRS also provides standard chromospheric activity indicators such as $\log R'_{\rm HK}$ and H_α. The DRS RV time-series has a root-mean-square of 54 m s^{-1} and a typical uncertainty of 2.0 m s^{-1}. Fig. 1 shows the DRS RV data with teal green hexagons (teal green colour will be used in this paper for all the DRS-related data/models). Table 2 contains all the time series described in this section.

[3] www.eso.org/sci/software/pipelines/espresso/ espresso-pipe-recipes.html

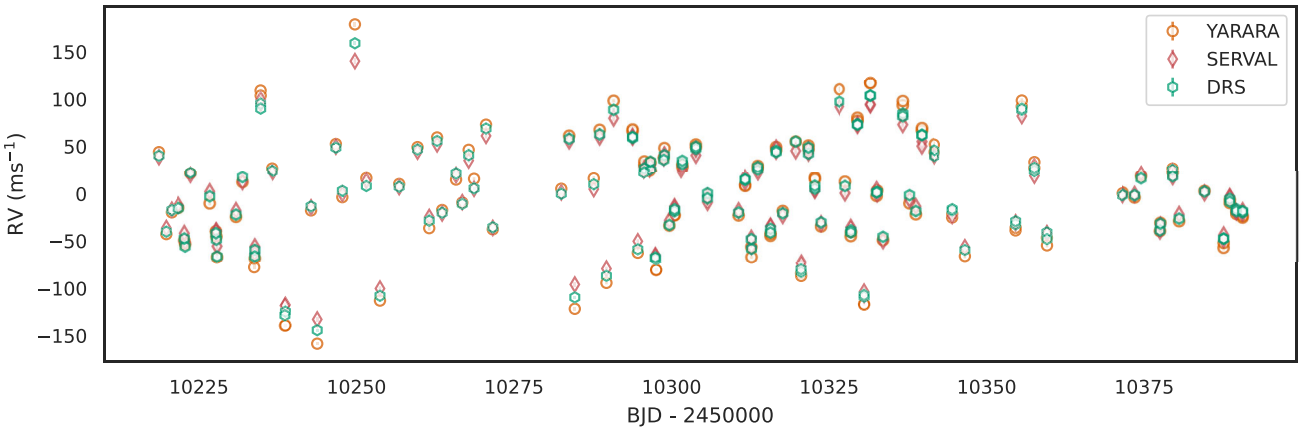

Figure 1. Mean-subtracted RV time-series as obtained with YARARA (vermilion circles), SERVAL (red diamonds), and DRS (teal green hexagons).

2.4.2 Yarara

YARARA is a post-processing methodology that aims to improve the RV extraction and RV precision by applying post-processing correction on the spectra time-series. Although primarily designed to search for m s^{-1} signals around Sun-like activity stars (M. Cretignier et al. 2023; M. Stalport et al. 2023; S. Dalal et al. 2024; N. Nari et al. 2025), the pipeline can be applied to any RV data sets and has been employed in Rossiter–McLaughin studies (H. Yu et al. 2025). Recently, YARARA has been upgraded to extract stellar atmospheric parameters (M. Cretignier et al. 2024).

During the pre-processing step, the S1D order-merged spectra from the official DRS are linearly interpolated on a common wavelength grid. The continuum of the spectra is then fitted by using RASSINE (M. Cretignier et al. 2020b). The fit of the continuum is mandatory to perform the colour correction as explained in M. Cretignier (2022) or O. Barragán et al. (2024b). We did not use the telluric correction of the pipeline since its effect is expected to be very small in comparison to the stellar activity signal. Furthermore, the CCF masks used later were designed to exclude spectral regions contaminated by telluric bands. Ultimately, only the cosmic ray correction was kept in the spectra cleaning process. Because the star is a moderate rotator, we did not try to perform a tailored line selection as that process requires narrow, well-separated lines (see M. Cretignier et al. 2020a). Instead, we used the standard G9 CCF mask of the ESPRESSO DRS to extract RVs and CCF momenta from the YARARA processed spectra. The main difference between the YARARA- and DRS-extracted RVs is that the former is done on the S1D spectra while the latter is done order by order. The YARARA RV time-series has a root-mean-square of 59 m s^{-1} and a typical uncertainty of 2.0 m s^{-1}. Fig. 1 shows the YARARA RV data as vermilion circles (vermilion colour will be used in this paper for all the YARARA-related data/models). Table 2 contains all the time series described in this section.

2.4.3 SERVAL

We also extracted RVs from the ESPRESSO spectra with SERVAL (M. Zechmeister et al. 2018). SERVAL computes a template spectrum from the observations themselves, rather than using a pre-existing digitised mask to compute the CCF as in the DRS. The template is constructed by co-adding the observed spectra in the barycentric rest-frame. For the reduction, we only use the orders from 10 to 160, since the rest have a relatively low signal-to-noise. The SERVAL analysis also produces time series of activity indicators, in this case we extracted the differential line width (DLW) and the chromatic index (CI) (see M. Zechmeister et al. 2018, for more details). The SERVAL RV time-series has a root-mean-square of 51 m s^{-1} and a typical uncertainty of 2.8 m s^{-1}. Fig. 1 shows the SERVAL RV data as red diamonds (red colour will be used in this paper for all the SERVAL-related data/models). Table 2 contains all the time series described in this section.

3 DATA ANALYSIS

3.1 Stellar parameters

Because of the high number of ESPRESSO spectra obtained in this work, we proceeded to estimate new stellar atmospheric and physical parameters. We also decided to adopt the stellar age of 125 ± 8 Myr found by N21 and stellar rotation of $P_{\rm rot} = 5.1 \pm 0.1$ d (O. Barragán et al. 2021; N21).

3.1.1 Atmospheric parameters

To obtain stellar atmospheric parameters for TOI-451, we used the combined spectrum from the YARARA-processed ESPRESSO observations, achieving an SNR of 568. We used the PAWS pipeline (A. V. Freckelton et al. 2024), which employs the functionality of the iSpec package (S. Blanco-Cuaresma 2019). The pipeline first determined initial estimates of the stellar parameters using the curve-of-growth equivalent widths method. These were used as input to the spectral synthesis method to subsequently determine the final atmospheric stellar parameters presented in Table 1. The atmospheric parameter set determined by the PAWS pipeline consists of $T_{\rm eff}$, $\log g$, [Fe/H], $v_{\rm mic}$, $v_{\rm mac}$, and $v \sin i$. Both methods in the PAWS pipeline were conducted using the SPECTRUM line list (R. O. Gray & C. J. Corbally 1994) and the ATLAS set of model atmospheres (R. L. Kurucz 2005).

3.1.2 TOI-451's mass and radius

To estimate TOI-451's mass and radius, we performed Spectral Energy Distribution (SED) modelling using the software ARI-

Table 1. Main identifiers and parameters for TOI-451.

Parameter	Value	Source
Main identifiers		
Gaia DR3	4844 691 297 067 063 424	G20
TYC	7577-172-1	E. Høg et al. (2000)
2MASS	J04115194-3756232	R. M. Cutri et al. (2003)
TESS Input Catalogue	257 605 131	K. G. Stassun et al. (2019)
Spectral type	G8V	This work
Equatorial coordinates, proper motion, and parallax		
α(J2000.0)	$04^{h}\,11^{m}\,51.9469^{s}$	G20
δ(J2000.0)	$-37^{h}\,56^{m}\,23.2192^{s}$	G20
μ_α (mas yr^{-1})	-11.061 ± 0.010	G20
μ_δ (mas yr^{-1})	12.347 ± 0.014	G20
π (mas)	8.0993 ± 0.0108	G20
Distance (pc)	123.47 ± 0.16	G20
Magnitudes		
B	11.64 ± 0.07	E. Høg et al. (2000)
V	10.94 ± 0.06	E. Høg et al. (2000)
Gaia G	10.7498 ± 0.0008	G20
J	9.636 ± 0.024	R. M. Cutri et al. (2003)
H	9.287 ± 0.022	R. M. Cutri et al. (2003)
K	9.190 ± 0.023	R. M. Cutri et al. (2003)
*W*1	9.137 ± 0.024	AllWISE
*W*2	9.173 ± 0.020	AllWISE
*W*3	9.117 ± 0.027	AllWISE
*W*4	8.632 ± 0.292	AllWISE
Stellar parameters		
$T_{\rm eff}$ (K)	5490 ± 115	This work
log g(cgs, dex)	4.53 ± 0.22	This work
[Fe/H] (dex)	0.02 ± 0.06	This work
$A_{\rm V}$	0.018 ± 0.016	This work
$v \sin i$ (km s^{-1})	8.70 ± 0.96	This work
$\sin i$	1.04 ± 0.13	This work
$v_{\rm mic}$ (km s^{-1})	0.97 ± 0.07	This work
$v_{\rm mac}$ (km s^{-1})	3.31 ± 0.11	This work
Luminosity, $L_\star$ ($L_\odot$)	0.59 ± 0.05	This work
Mass, $M_\star$ ($M_\odot$)	0.93 ± 0.04	This work
Radius, $R_\star$ ($R_\odot$)	0.85 ± 0.03	This work
Density, $\rho_\star$ (g cm^{-3})	2.15 ± 0.25	This work
$P_{\rm rot}$ (d)	5.1 ± 0.1	This work
Age (Myr)	125 ± 8	N21

Note. G20 corresponds to Gaia Collaboration (2020).

Table 2. Stellar time series. Columns list, in order, the observation time, the measured value, the associated uncertainty, the physical units, and a label. The label (fifth column) specifies both the measured quantity (e.g. NGTS photometry, RV serval, FWHM, etc). The full table is provided in machine-readable format in the supplementary material.

Time BJD$_{\rm TDB}$ − 2450 000)	Value	$\sigma_{\rm Value}$	Units	Time-series
10218.692220	0.05559	0.00200	km s^{-1}	RV serval
10219.863082	−0.01920	0.00236	km s^{-1}	RV serval
10220.738287	0.00016	0.0040	km s^{-1}	RV serval
10221.758381	0.00447	0.00178	km s^{-1}	RV serval
10222.856319	−0.03405	0.00199	km s^{-1}	RV serval
-	-	-	-	-

ADNE (J. I. Vines & J. S. Jenkins 2022). We used four stellar atmospheric models: `Phoenix v2` (T. O. Husser et al. 2013), `BtSettl` (F. Allard, D. Homeier & B. Freytag 2012), F. Castelli & R. L. Kurucz (2004), and R. L. Kurucz (1993) to model TOI-451's SED. We used broad-band photometry from 2MASS *J*, *H*, and *K*, *WISE W*1 and *W*2, the *Johnson B* and *V* magnitudes, and *Gaia* G magnitude and parallax from *Gaia* DR3 (see Table 1). The parameter space was explored used the nested sampling algorithm implemented in `dynesty` (J. S. Speagle 2020). We set Gaussian priors for $T_{\rm eff}$, log g, [Fe/H], and distance from our atmospheric analysis (see Table 1). Stellar radius ($R_\star$) and extinction (A_V) were treated as free parameters. We obtained $R_\star = 0.85 \pm 0.03\,R_\odot$ and $A_v = 0.018 \pm 0.016$ mag. `ARIADNE` also estimated a stellar mass of $M_\star = 0.93 \pm 0.04\,M_\odot$ using the `isochrones` package with the MIST stellar evolution tracks (T. D. Morton 2015; J. Choi et al. 2016). The corresponding results are summarized in Table 1.

To cross-check the `ARIADNE` results, we also used the `PARAM 1.3` [4] online calculator. We used the $T_{\rm eff}$ and [Fe/H] values from our spectroscopic analysis together with the visual magnitude and parallax given in Table 1 as input for `PARAM 1.3`. Given the well-constrained age of this star given by N21, we set stellar age priors between 100 and 150 Myr and the `PARSEC` isochrones (A. Bressan et al. 2012). We recovered a mass and radius of $M_\star = 0.96 \pm 0.02\,M_\odot$ and $R_\star = 0.83 \pm 0.02\,R_\odot$. These results are in agreement with our `ARIADNE` estimates and N21.

3.2 Transit analysis

The transit modelling includes the photometric data from *TESS* and NGTS described in Section 2. To enhance computational efficiency, we constrain the analysis to temporal windows encompassing up to three hours on either side of each transit midpoint. Given that the *TESS* and NGTS time-series were acquired with short cadences (less than 2 min), the light curves can be accurately represented by instantaneous evaluations of the transit models (cf., e.g. D. Gandolfi et al. 2018).

To model the transits of TOI-451 b, c, and d, we need to sample and set priors for the following parameters for each planet: time of mid-transit, T_0; orbital period, $P_{\rm orb}$; orbital eccentricity, e, angle of periastron, $\omega_\star$; and the scaled planetary radius $R_{\rm p}/R_\star$. We also sample for the stellar density, $\rho_\star$; and the limb darkening parameters q_1 and q_2 for each band (following K. Mandel & E. Agol 2002; D. M. Kipping 2013, models and parametrizations). The scaled semimajor axis for each planet, $a/R_\star$, is recovered from $\rho_\star$ and Kepler's third law (see e.g. J. N. Winn 2010). The model also includes a photometric jitter term per data set to penalise the likelihood. We assume circular orbits for all planets.

We set wide uniform priors for all the parameters based on previous analyses and physical boundaries. For all the subsequent analyses, we used `pyaneti` (O. Barragán, D. Gandolfi & G. Antoniciello 2019a; O. Barragán et al. 2022a). In all our runs, we sample the parameter space with 250 walkers using the Markov chain Monte Carlo (MCMC) ensemble sampler algorithm implemented in `pyaneti` which is based on D. Foreman-Mackey et al. (2013). We ran the MCMC and check for convergence each 5000 iterations. We define convergence when the A. Gelman & D. B. Rubin (1992) statistics is less than 1.01. Once convergence is reached, posterior distributions are created with the last 5000 iterations of converged chains. Chains are thinned by a factor of 10, giving a distribution of 125 000 points for each sampled parameter.

Fig. 2 shows the phase-folded transit data and inferred models for the three planets. The major advantage of the inclusion of the NGTS data is that it improves the ephemerides for TOI-451 c and d in comparison with the latest estimates of the system (2 to 3 times more precise). These new observations also show that there are no significant long-term transit time variations in the system. This is of high importance for future transit observations.

[4] http://stev.oapd.inaf.it/cgi-bin/param_1.3

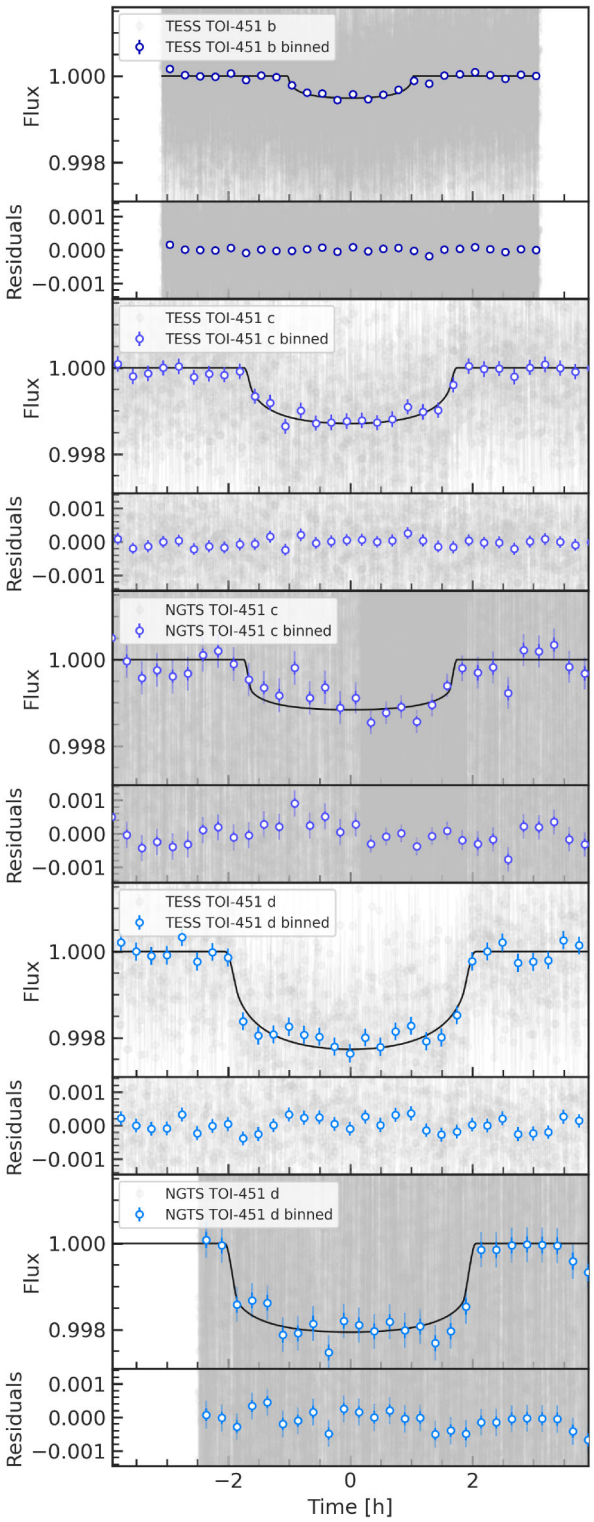

Figure 2. Detrended light curves phase-folded at the period of each planet (individual data points in transparent grey, phase-binned data in solid colour) together with the best-fitting transit model (black line). Residuals are shown in the lower inset. The *x*- and *y*-axes in each panel are shown with the same range to facilitate signal comparisons.

We use the results from the transit modelling as priors for our analyses of the RVs, which are presented in Section 3.4. The final inferred and derived transit parameters are given in Section 3.5.

3.3 Stellar time-series characterization

3.3.1 Periodograms

As a first check to test the information contained in our stellar time-series, we ran a General Lomb–Scargle (GLS; M. Zechmeister & M. Kürster 2009) periodogram on them. Fig. 3 shows the GLS periodogram of all the contemporaneous stellar time-series described previously. We can see that most of them peak around 2.5 and 1.7 d, which correspond to the first and second harmonics of the stellar rotation period ($P_{\rm rot} \sim 5.1$ d; see O. Barragán et al. 2021; N21). This suggests that the stellar signal contained in the time series has relatively high harmonic complexity. We note that the chromospheric activity indicators ($\log R'_{\rm HK}$ and $\rm H_\alpha$) and the SERVAL DLW do not have significant peaks. This suggests that these time series are not dominated by rotational signals or other periodic phenomena.

We also searched for evidence of the planetary signals in the raw RV time series. We found no substantial peaks corresponding to the orbital period of TOI-451 b, c, and d in any of the RV time series. This is expected given the relatively large activity-induced variations in comparison with the expected small Doppler semi-amplitudes of the planets.

3.3.2 Gaussian processes

We performed several analyses of the light curve and spectroscopic time-series to analyse and characterize the time-scales over which the stellar signal evolves. Hereafter, we will only show the results obtained from the SERVAL time-series, DRS CCF activity indicators, two chromospheric indicators ($\rm H_\alpha$ and $\log R'_{\rm HK}$) and LCO and NGTS light curves. We note that we performed similar analyses with the DRS and YARARA RV time-series, obtaining similar results. We choose to present the results of the SERVAL RVs because they have the smaller peak-to-peak variations (see Section 2.4).

We first perform 1D GP regressions on the different contemporaneous activity indicators and light curves. Given the quasi-periodic nature of the stellar signal, we describe the covariance between two data points at times t_i and t_j for each time-series using

$$\gamma_{\rm 1D} = A^2 \gamma_{i,j}, \tag{1}$$

where A represents the amplitude factor, and $\gamma_{i,j}$ is given by the quasi-periodic (QP) kernel

$$\gamma_{{\rm QP},i,j} = \exp\left[-\frac{\sin^2[\pi (t_i - t_j)/P_{\rm GP}]}{2\lambda_{\rm P}^2} - \frac{(t_i - t_j)^2}{2\lambda_{\rm e}^2} \right], \tag{2}$$

where the hyperparameters are: $P_{\rm GP}$, which is the characteristic GP period; $\lambda_{\rm P}$, controlling harmonic complexity; and $\lambda_{\rm e}$, which is the evolution time-scale.

For each run, we sample six parameters: the four kernel hyperparameters (A, $P_{\rm GP}$, $\lambda_{\rm e}$, $\lambda_{\rm P}$), one offset as the mean function, and an additional jitter term added to the diagonal of the covariance matrix. We use broad uniform priors for these parameters with the following ranges: For $\lambda_{\rm e}$ between 0.1 and 100 d (half the observational window); for $\lambda_{\rm P}$ between 0.1 and 5 (0.1 corresponds

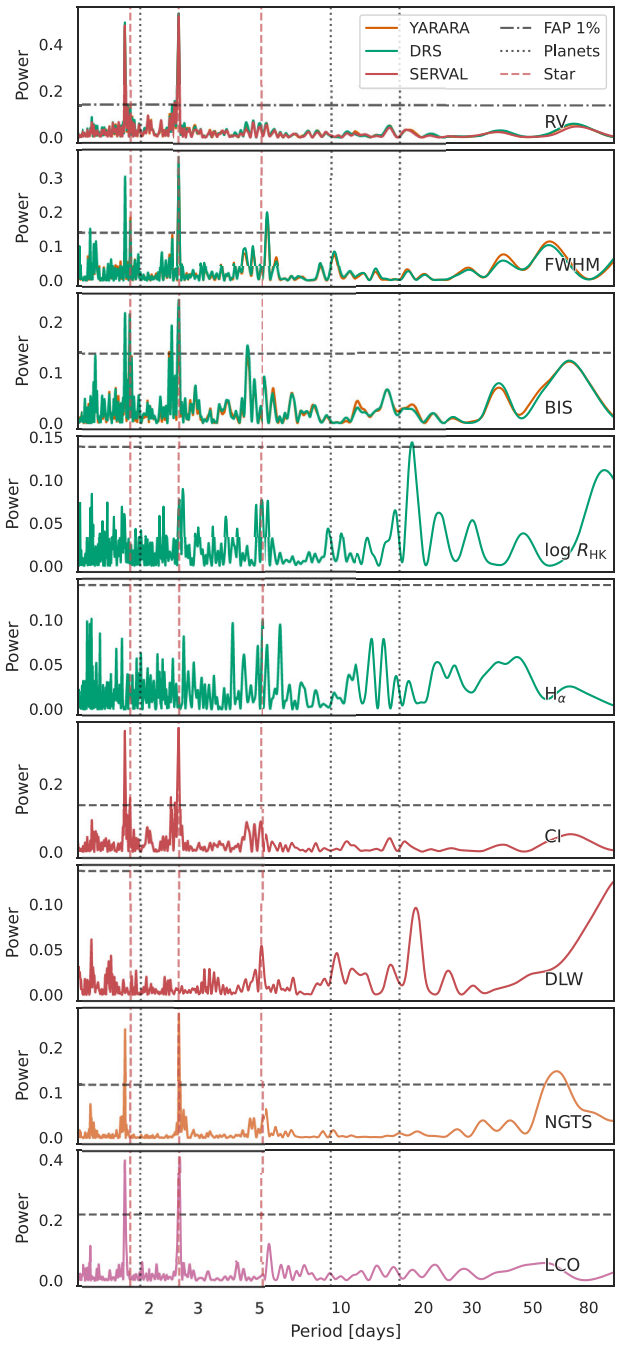

Figure 3. GLS periodograms of the stellar time-series. The horizontal dashed line indicates the 1 per cent False Alarm Probability (FAP). The vertical red dashed lines represent the fundamental, first and second harmonics of the rotation period of the star stellar-related signals, while the vertical black dotted lines mark the orbital periods of TOI-451 b, c, and d.

to high harmonic complexity and 5 to a quasi-coherent signal), and for P_{GP} between 4.8 and 5.3 d (to include the expected stellar period from the *TESS* photometry). The parameter space is explored using the MCMC sampler built into `pyaneti`, following the same MCMC set-up outlined in Section 3.2.

Table 3 shows the inferred P_{GP}, λ_e, and λ_p hyperparameters for all the stellar time-series. Fig. 4 shows the TOI-451 stellar time-series with the inferred GP model. Fig. 5 and Table 3 summarize the inferred posterior distributions for the P_{GP}, λ_e, and λ_p parameters for all the runs.

Table 3. Recovered hyperparameters for 1D GP regression for different stellar time-series.

Time-series	P_{GP} [d]	λ_e [d]	λ_p
RV	$5.15^{+0.01}_{-0.01}$	$24.6^{+3.9}_{-3.7}$	$0.18^{+0.02}_{-0.02}$
DRS FWHM	5.13 ± 0.01	$21^{+3.4}_{-3.8}$	$0.14^{+0.02}_{-0.02}$
DRS BIS	5.13 ± 0.01	$24^{+4.2}_{-3.9}$	$0.13^{+0.02}_{-0.01}$
Serval contrast	$5.14^{+0.01}_{-0.02}$	$37^{+12}_{-8.3}$	$0.22^{+0.04}_{-0.04}$
LCO	5.17 ± 0.03	$31^{+12}_{-7.9}$	$0.48^{+0.28}_{-0.21}$
NGTS	5.05 ± 0.02	$13^{+1.5}_{-1.6}$	$0.38^{+0.04}_{-0.04}$
NGTS sub.	5.10 ± 0.02	16 ± 1.6	$0.38^{+0.04}_{-0.04}$

We first discuss the results on the parameter P_{GP}, which is related to the rotation period of the star. The first thing to note is that the chromospheric activity indicators ($\log R'_{HK}$ and H_α) and the `SERVAL` DLW do not have a constrained solution for the period (as also indicated in the periodogram analysis). Their posterior distribution, as seen in Fig. 5, is constrained purely from the uniform prior, indicating that the inferred values are not constrained by the data. Therefore we do not include their inferred parameters in Table 3. A possible reason for this is the relatively low signal-to-noise of each spectrum, resulting in fairly noisy estimates of these quantities measurements with relatively high noise. Such relatively high noise degrades our ability to recover patterns in the data (see also discussion in O. Barragán et al. 2023). The RV, CCF activity indicators, the light curves, and `SERVAL` CI provide a constrained period that peaks around 5.1 d. All the posteriors are consistent with each other within 1σ except for the NGTS light curve (see Fig. 5). The period recovered from the latter is 3σ away from that obtained from the other stellar time-series. We note that, as shown in Fig. 4, the NGTS data starts approximately 50 d before the ESPRESSO observations, corresponding to $\sim$10 rotations of the star, during which the active regions evolved significantly. This could explain the lower P_{GP} and λ_e measured in the NGTS light curve. To test this hypothesis, we modelled a subset of the NGTS data that starts at the same time as the ESPRESSO observations, which we will call NGTS sub. We ran the same 1D GP set-up discussed in this section. Figs 4 and 5 show that for NGTS sub., the recovered P_{GP} is fully consistent with the rest of the contemporaneous stellar time-series. From these results, we conclude that the RVs, the CCF activity indicators, the light curves, and the `SERVAL` CI all trace rotationally modulated features of the stellar surface.

We continue by analysing the parameter λ_e, which quantifies the coherence of the periodic signal and is related to the lifetime of the active regions (B. A. Nicholson & S. Aigrain 2022). The first thing to notice in Table 3 is that the value of λ_e is at least twice the value of P_{GP} for all the time-series with detected P_{GP}. This implies that the local coherence of the periodic signal is maintained for at least two stellar rotations. On the other hand, Table 3 shows a wide range of values for λ_e for the different time-series. A possible explanation for this is that the different time series are sensitive to different types of surface features with different lifetimes (as seen also for Sun-like stars, see B. Klein et al. 2024). O. Barragán et al. (2023) also noticed that relatively low signal-to-noise time-series can give larger λ_e values. This is because low signal to noise time-series are less sensitive to small evolutionary changes in the

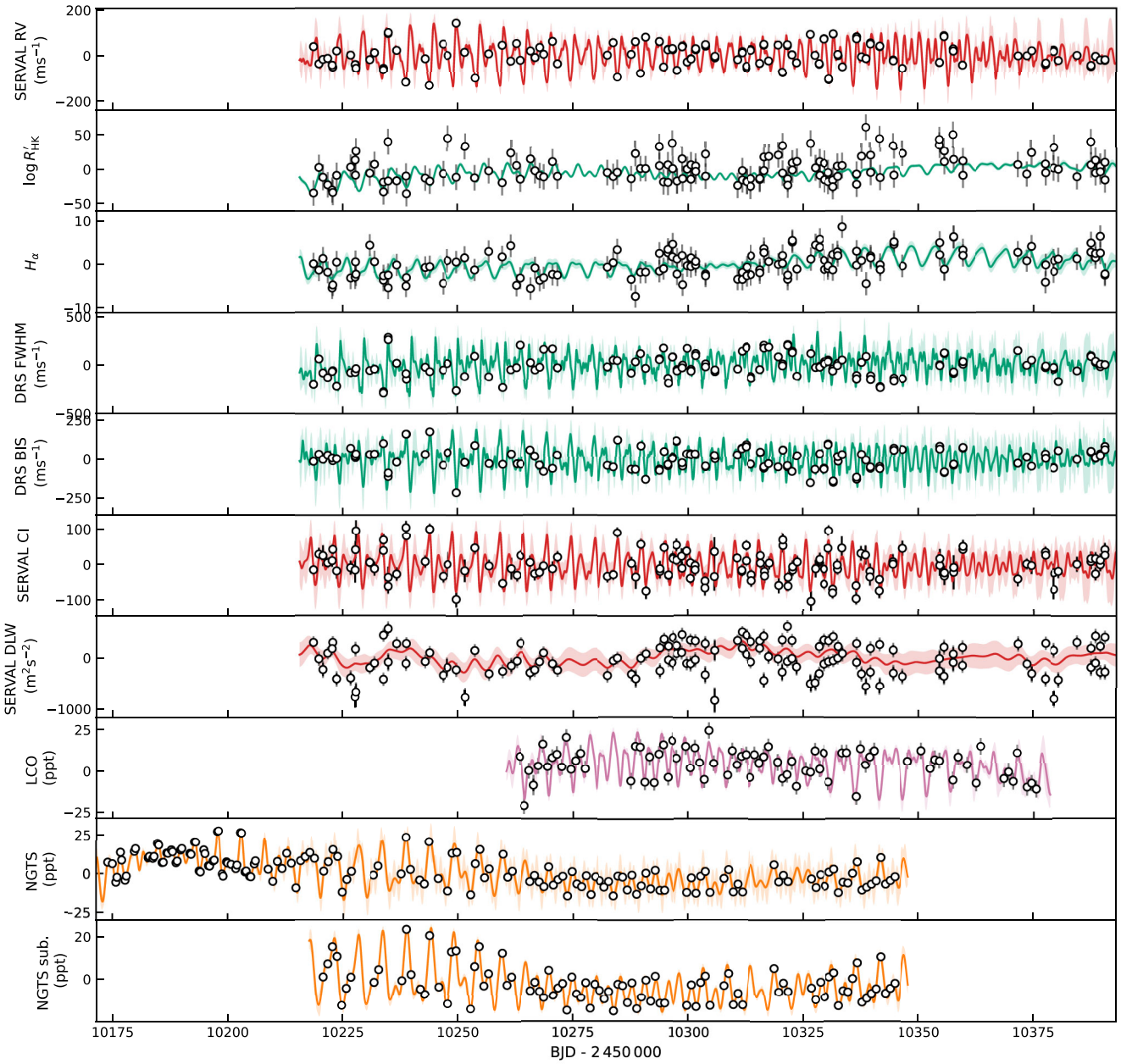

Figure 4. 1D GP regression on each of the contemporaneous TOI-451 time-series. Measurements are shown as black circles with error bars, with semitransparent extension accounting for the inferred jitter. Solid coloured lines show the posterior predictive mean and 3σ credible interval of the inferred GP model.

signals, and larger λ_e values are favoured by the GP's built-in Occam's razor.[5]

Finally, we examine the complexity of the inferred stellar signal, as quantified by the parameter λ_p, which can be understood as the length scale of the periodic signal. It is expected that *RV-like* time-series (i.e. those that depends on the change of location of the active regions from the red- to the blue-shifted stellar hemisphere, and vice-versa, like the RV or BIS) should have a higher harmonic complexity than the *photometry-like* (i.e. those which are good tracers of the areas covered by active regions on the stellar surface) in 1D GP regressions (as expected from the FF' framework of S. Aigrain et al. 2012; see also O. Barragán et al. 2022a, 2023). We would thus expect that the RV and BIS would yield a relatively small λ_p value compared to the *photometry-like* time-series. This relation is not observed for all the time-series in Table 3 and Fig. 5. As a comparison point, we can take the λ_p value obtained from the RV time series. Most notoriously, FWHM gives a significantly smaller $\lambda_p$than the RVs. O. Barragán et al. (2024b) presented a similar case of unexpected λ_p values for FWHM, and argued that this is due to overfitting. These kinds of results indicate an overfit of the data where the white noise is fitted as fast evolving red noise (behaviour caused by small values of

[5]Larger values of λ_e reduce the determinant of the covariance matrix $|\mathbf{K}|$, and the GP likelihood includes $|\mathbf{K}|^{-1}$.

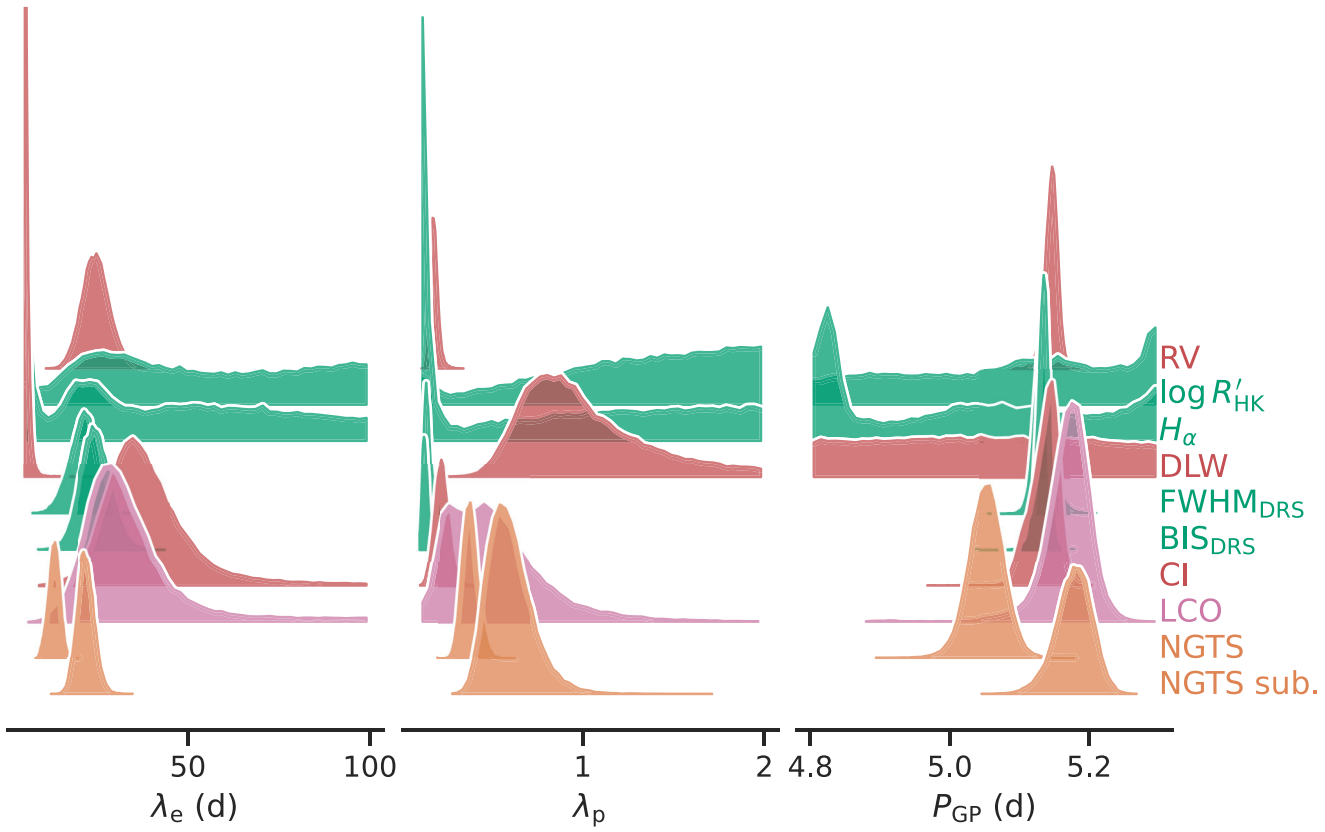

Figure 5. Posterior distributions for P_{GP}(left), λ_e (centre), and λ_p (right). Different time-series results are differentiated with a label and offset.

λ_p). The risk of overfitting is compounded in the present case by the high harmonic complexity of the signal (already noted from the GLS periodogram analysis in Section 3.3.1), by the relatively sparse separated data compared to TOI-451's short rotation period and by the rapid evolution of the signal (O. Barragán et al. 2021) compared to the gaps in the observations. These results hint that the activity indicators extracted from the ESPRESSO observations may be of limited use to characterize the stellar signal and separate it from the planetary signals, because all these time series suffer from the same, relatively poor time-sampling. From Fig. 4 we can see how the FWHM, BIS, and `SERVAL` CI predictive distributions evolve relatively fast compared to the gaps between consecutive points. This behaviour is characteristic of overfitting (see O. Barragán et al. 2023; S. Blunt et al. 2023).

The NGTS and LCO light curves give λ_p values that are consistently larger than those obtained from the RVs, but this is what we expect from the FF' framework. This is because they have a better sampling than the spectroscopic time series. The λ_p values obtained from these light curves are more reliable, as they have better time-sampling than the spectroscopic time-series. From Fig. 4 we can see that the light curves evolve more smoothly, similarly to the *TESS* light curves from previous seasons (O. Barragán et al. 2021).

From this detailed 1D GP analysis, we can conclude that the stellar signal seems better characterized by the light curves than the ESPRESSO time-series. The most important variables that determine the ability to characterize the signal are the signal-to-noise ratio and the time sampling. The latter must be tight compared to the evolutionary time-scales of the signal, both periodic and long-term (see discussion in O. Barragán et al. 2024b). These two criteria are better kept in our light curves. In the next section, we explore how different combinations of these time series affect our ability to recover the planetary signals.

3.4 RV planetary analysis

We now proceed to run diverse multi-GP models where we include the signal of the three transiting planets in the RV time-series and model the stellar signal of each time series as a linear combination of a single latent GP and its time derivative (see V. Rajpaul et al. 2015; O. Barragán et al. 2022a, for more details). For all our runs, we use the QP kernel shown in Section 3.3 and its corresponding derivatives (V. Rajpaul et al. 2015; O. Barragán et al. 2022a). We modified the `pyaneti` version presented in O. Barragán et al. (2019a) to allow for modelling of contemporaneous time-series with different time stamps and number of observations.

We create $N-$dimensional GP models, including N time-series $\mathcal{A}_i$, as

$$\begin{aligned} \mathcal{A}_1 &= A_1 G(t) + B_1 \dot{G}(t) \\ &\vdots \\ \mathcal{A}_N &= A_N G(t) + B_N \dot{G}(t), \end{aligned} \tag{3}$$

where the parameters $A_1, B_1, \ldots, A_N, B_N$ serve as free coefficients that connect each time-series to both $G(t)$ and its time derivative, $\dot{G}(t)$. In this framework, $G(t)$ represents an unobserved (latent) variable, which can be conceptually understood as the time-

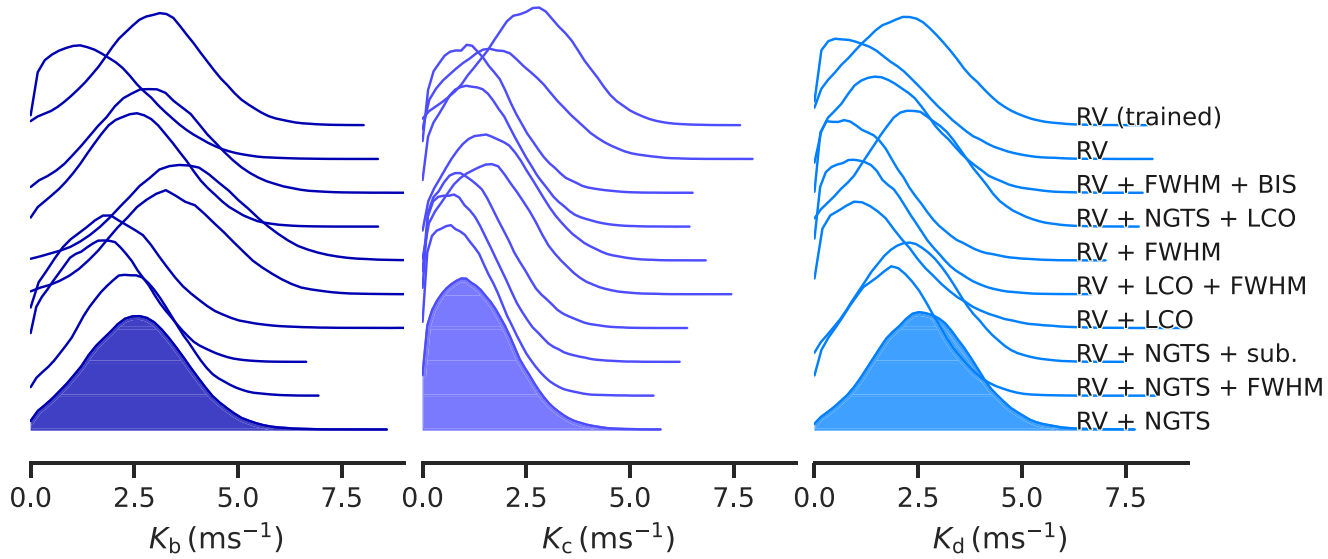

Figure 6. Posterior distributions for the Doppler semi-amplitudes for TOI-451 b, c, and d. Each posterior distribution corresponds to a different model labelled to the right. We highlight the adopted distributions (RV + NGTS) in this work with a coloured filled distribution.

dependent coverage of active regions across the projected visible stellar disc.

We model the RV and BIS as *RV-like* time series that are described by $G(t)$ and $\dot{G}(t)$, while the rest of the time series are assumed *photometry-like*, i.e. modelled only by $G(t)$.

The mean function for the RV time-series consists of the planetary signals. We use three Keplerian signals, where every Keplerian signal i is parametrized by a time of minimum conjunction (equivalent to the time of mid-transit for transiting planets), $T_{0,i}$; orbital period, $P_{\mathrm{orb},i}$; orbital eccentricity, e_i; angle of periastron, $\omega_{\star,i}$; and Doppler semi-amplitude, K_i. We also include one offset and a jitter term to penalise the imperfections of our model.

We first ran 1D GP models on the RV time-series only, following the same set-up as described in Section 3.3. We ran two different flavours of RV-only model: one with uniform priors for all the GP hyper-parameters, and one with a GP trained with the NGTS light curve (i.e. using the values of Table 3 for NGTS sub.). We also performed multi-GP regressions using different combinations of RV and activity indicators and/or light curves. We used the same MCMC set-up as the one described in Section 3.2. We set Gaussian priors on the planet ephemerides based on the results obtained in Section 3.2. We set uniform priors for the reminder parameters. We also assumed circular orbits for the three planets. For all the GP hyperparameters, we set uniform priors with the same ranges described in Section 3.3 (except for the GP-trained case in which we set Gaussian priors).

Fig. 6 shows the posterior distributions of the Doppler semi-amplitudes of TOI-451 b, c, and d for all the multi-GP runs. Interestingly, the approach employing the 1D GP training delivers the most precise outcomes alongside 3σ detections. Although this result might appear preferable, we need to cautious, as such detections may be caused by overfitting, by forcing covariances that are not representative of the intrinsic covariance in the RV. By visually inspecting the inferred posterior distributions, we cannot distinguish which one gives the better value or the most precise. All inferred posteriors give distributions that agree well with each other. Following the suggestions of V. M. Rajpaul, O. Barragán & N. Zicher (2024), the present analysis shows that diverse activity models produce consistent results, suggesting that the true Doppler semi-amplitudes reside within the inferred credible intervals.

We conclude that it is not possible to obviously distinguish which method provides the optimal model for adoption in this work. To differentiate between methods and identify the best model would require a quantitative comparison of the various multi-GP models, which lies beyond the scope of this manuscript. To select the final model to use in this manuscript, we refer to our results from the one-dimensional GP regressions of the stellar time series (Section 3.3.2). We concluded that the ESPRESSO spectroscopic activity indicators fail to constrain the stellar activity signal robustly by themselves. Meanwhile, the NGTS/LCO light curves successfully constrain the time-scales of the stellar signal by themselves. Therefore, we adopt the two-dimensional GP regression of RV + NGTS as our final model. We select the NGTS over the LCO observations because they cover a larger time span.

3.5 Final joint model

For completeness, we ran a final joint model of transit photometry and RV to characterize TOI-451's planetary signals. Based on the analyses presented in this section, our final model for TOI-451 is the transit model described in Section 3.2, together with the RV-NGTS multi-GP model described in Section 3.4. The whole set of sampled parameters and priors are shown in Table 4.

We also re-run the same model, but this time allowing for eccentric orbits for the three planets. We obtained Doppler semi-amplitudes consistent with the circular orbit case with $k_b = 2.7 \pm 1.2\,\mathrm{m\,s^{-1}}$, $k_c = 1.4^{+1.2}_{-0.9}\,\mathrm{m\,s^{-1}}$, and $k_d = 2.9 \pm 1.4\,\mathrm{m\,s^{-1}}$, with corresponding eccentricities of $e_b = 0.15^{+0.16}_{-0.10}$, $e_b = 0.21^{+0.28}_{-0.16}$, and $e_d = 0.09^{+0.13}_{-0.07}$. These eccentricities cannot be distinguished from circular orbits. This result is supported by a Akaike Information Criterion difference of 13 on favour of the circular orbits model. We therefore conclude that our data set does not allow us to set

Table 4. Sampled parameters and priors for final modelling.

Parameter	Prior [a]	Final value [b]	Maximum value [c]
TOI-451 b's parameters			
Orbital period $P_{\rm orb}$ (days)	$\mathcal{U}[1.8586, 1.8589]$	$1.8587033^{+0.0000093}_{-0.0000114}$	-
Transit epoch T_0 (BJD$_{\rm TDB}-2450\,000$)	$\mathcal{U}[10312.3110, 10312.5110]$	$10312.4427^{+0.0067}_{-0.0090}$	-
Scaled planet radius $R_{\rm p}/R_\star$	$\mathcal{U}[0.0, 0.05]$	0.01983 ± 0.00072	-
Impact parameter, b	$\mathcal{U}[0, 1]$	$0.16^{+0.16}_{-0.11}$	-
Orbital eccentricity, e	$\mathcal{F}[0]$	0	-
Angle of periastron, $\omega_\star$ (deg)	$\mathcal{F}[90]$	90	-
Doppler semi-amplitude variation K (m s^{-1})	$\mathcal{U}[0, 50]$	$2.6^{+1.1}_{-1.2}$	5.3
TOI-451 c's parameters			
Orbital period $P_{\rm orb}$ (days)	$\mathcal{U}[9.1920, 9.1930]$	9.192463 ± 0.000017	-
Transit epoch T_0 (BJD$_{\rm TDB}-2450\,000$)	$\mathcal{U}[10314.5279, 10314.7279]$	10314.6376 ± 0.0025	-
Scaled planet radius $R_{\rm p}/R_\star$	$\mathcal{U}[0.0, 0.05]$	0.03166 ± 0.00078	-
Impact parameter, b	$\mathcal{U}[0, 1]$	$0.26^{+0.14}_{-0.16}$	-
Orbital eccentricity, e	$\mathcal{F}[0]$	0	-
Angle of periastron, $\omega_\star$ (deg)	$\mathcal{F}[90]$	90	-
Doppler semi-amplitude variation K (m s^{-1})	$\mathcal{U}[0, 50]$	$1.2^{+1.0}_{-0.8}$	3.7
TOI-451 d's parameters			
Orbital period $P_{\rm orb}$ (days)	$\mathcal{U}[16.3648, 16.3651]$	16.364962 ± 0.000015	-
Transit epoch T_0 (BJD$_{\rm TDB}-2450\,000$)	$\mathcal{U}[10314.8635, 10315.0635]$	10314.9694 ± 0.0014	-
Scaled planet radius $R_{\rm p}/R_\star$	$\mathcal{U}[0.0, 0.05]$	$0.04243^{+0.00078}_{-0.00073}$	-
Impact parameter, b	$\mathcal{U}[0, 1]$	$0.382^{+0.085}_{-0.095}$	-
Orbital eccentricity, e	$\mathcal{F}[0]$	0	-
Angle of periastron, $\omega_\star$ (deg)	$\mathcal{F}[90]$	90	-
Doppler semi-amplitude variation K (m s^{-1})	$\mathcal{U}[0, 50]$	2.7 ± 1.2	5.5
GP hyperparameters			
GP Period $P_{\rm GP}$ (days)	$\mathcal{U}[4.9, 5.3]$	$5.078^{+0.021}_{-0.020}$	-
$\lambda_{\rm p}$	$\mathcal{U}[0.1, 5]$	$0.363^{+0.025}_{-0.022}$	-
$\lambda_{\rm e}$ (days)	$\mathcal{U}[5, 100]$	11.5 ± 1.2	-
$A_{\rm RV}$ (m s^{-1})	$\mathcal{U}[0, 100]$	$6.1^{+3.0}_{-3.1}$	-
$B_{\rm RV}$ (m s^{-1} d^{-1})	$\mathcal{U}[-100, 100]$	$28.0^{+3.5}_{-2.8}$	-
$A_{\rm NGTS}$ (ppm)	$\mathcal{U}[-100, 100]$	$-8.6^{+0.8}_{-1.0}$	-
$B_{\rm NGTS}$ (ppm d^{-1})	$\mathcal{F}[0]$	0	-
Other parameters			
Stellar density $\rho_\star$ (g cm^{-3})	$\mathcal{U}[0.1, 5]$	$1.84^{+0.20}_{-0.22}$	-
TESS limb-darkening coefficient q_1	$\mathcal{U}[0, 1]$	$0.35^{+0.26}_{-0.15}$	-
TESS limb-darkening coefficient q_2	$\mathcal{U}[0, 1]$	$0.40^{+0.34}_{-0.24}$	-
NGTS limb-darkening coefficient q_1	$\mathcal{U}[0, 1]$	$0.21^{+0.24}_{-0.14}$	-
NGTS limb-darkening coefficient q_2	$\mathcal{U}[0, 1]$	$0.35^{+0.38}_{-0.25}$	-
Offset RV (km s^{-1})	$\mathcal{U}[-1, 1]$	$0.0157^{+0.0029}_{-0.0031}$	-
Offset NGTS	$\mathcal{U}[0.9, 1.1]$	1.0012 ± 0.0018	-
Jitter term $\sigma_{\rm RV}$ (m s^{-1})	$\mathcal{J}[1, 100]$	$2.9^{+1.1}_{-0.9}$	-
Jitter term $\sigma_{\rm NGTS}$ (ppm)	$\mathcal{J}[1, 100]$	$1.39^{+0.21}_{-0.20}$	-

[a] $\mathcal{F}[a]$ refers to a fixed value a, $\mathcal{U}[a, b]$ to an uniform prior between a and b, and $\mathcal{J}[a, b]$ to the modified Jeffrey's prior as defined by P. C. Gregory (2005, equation 16).
[b] Inferred parameters and errors are defined as the median and 68.3 per cent credible interval of the posterior distribution.
[c] Maximum values reported as the 99 per cent upper credible limit.

constrains on the eccentric orbits of the planets and we adopt the model with circular orbits.

Fig. 7 shows the RV and NGTS time-series, together with the phase-folded planetary Doppler signal. Table 4 shows the inferred sampled parameters, defined as the median and 68.3 per cent credible interval of the posterior distribution. Table 5 also shows the derived planetary and orbital parameters.

4 DISCUSSION

4.1 Injection tests

It has been shown that the combination of complex models and the window function of the observations can create spurious planet-like signals in RV time-series, specially for active stars (e.g.

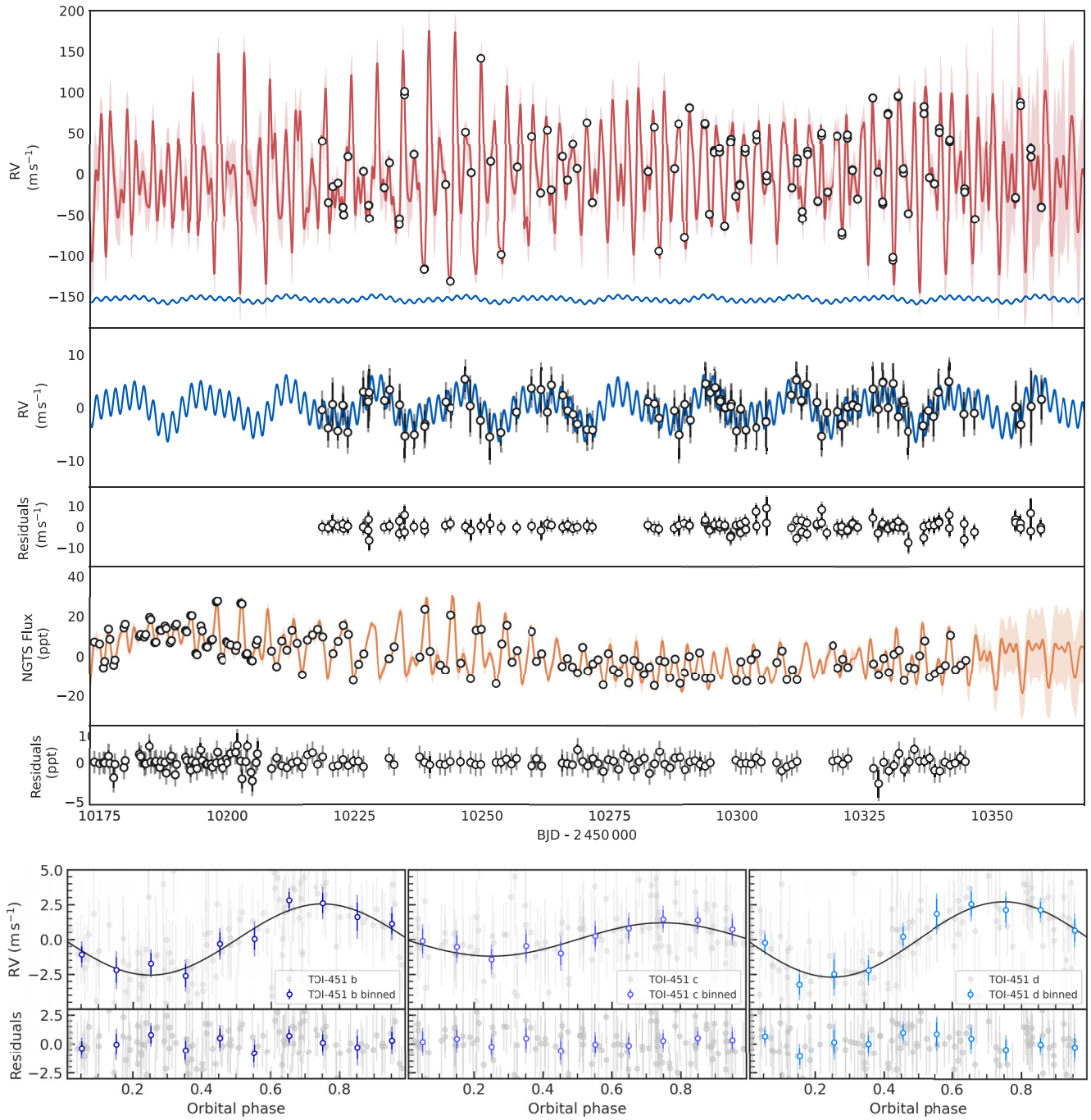

Figure 7. *Top:* TOI-451's RV and NGTS time-series after being corrected by inferred offsets. The plot shows (from top to bottom) RV data together with full and planetary signal inferred models; RV data with stellar signal model subtracted; RV residuals; NGTS data together with inferred stellar model, and NGTS residuals. The solid lines show the inferred full model coming from our multi-GP, light-shaded areas showing the corresponding GP model's 3σ credible intervals. *Bottom:* Phase-folded RV signals for TOI-451 b, c, and d following the subtraction of the systemic velocities, stellar signal, and other planets. Nominal RV observations are shown as light grey points. Solid colourful points show binned data to 1/10 of the orbital phase.

V. Rajpaul, S. Aigrain & S. Roberts 2016). In order to check the reliability of our RV detection, we performed numerical simulations similar to O. Barragán et al. (2019b) and N. Zicher et al. (2022), and suggested by V. M. Rajpaul et al. (2024).

We use `citlalatonac` (O. Barragán et al. 2022a) to simulate synthetic RV and NGTS time-series. We utilize the median predictive distribution obtained from the multi-GP model for each of this time series as the base of our stellar signal. We then added correlated noise, to mimic instrumental systematics, as a GP generated by a squared exponential kernel with a length-scale of one day, and the same amplitude as the jitter term obtained from the real data for each time series. We then use the same time stamps from the real observations to create synthetic data, and added white noise for each synthetic datum according to the nominal

Table 5. Derived parameters for the TOI-451 planets.

Parameter	TOI-451 b's values	TOI-451 c's values	TOI-451 d values
Planet mass M_p ($M_\oplus$)	$4.7^{+2.1}_{-2.2}$	$3.7^{+3.2}_{-2.4}$	$10.2^{+4.6}_{-4.5}$
Maximum planet mass ($M_\oplus$)[a]	9.7	11.5	20.7
Planet radius R_p ($R_\oplus$)	1.84 ± 0.11	2.93 ± 0.16	3.93 ± 0.20
Planet density ρ_p (g cm^{-3})	$4.1^{+2.2}_{-1.9}$	$0.81^{+0.72}_{-0.53}$	$0.92^{+0.46}_{-0.41}$
Scaled semimajor axis $a/R_\star$	$6.95^{+0.24}_{-0.29}$	$20.18^{+0.70}_{-0.85}$	$29.6^{+1.0}_{-1.3}$
Semimajor axis a (au)	0.0274 ± 0.0017	0.0795 ± 0.0050	$0.1168^{+0.0072}_{-0.0074}$
Orbit inclination i_p (°)	$88.7^{+0.9}_{-1.4}$	$89.27^{+0.47}_{-0.43}$	89.26 ± 0.20
Transit duration τ_{14} (hours)	$2.059^{+0.066}_{-0.078}$	$3.461^{+0.086}_{-0.078}$	$4.094^{+0.050}_{-0.045}$
Planet surface gravity g_p (cm s^{-2})[b]	1210^{+576}_{-573}	380^{+328}_{-248}	576^{+276}_{-255}
Planet surface gravity g_p (cm s^{-2})[c]	1352^{+658}_{-635}	426^{+368}_{-278}	645^{+307}_{-286}
Equilibrium temperature T_{eq} (K)[d]	1474^{+45}_{-40}	865^{+27}_{-24}	714^{+22}_{-19}
Received irradiance ($F_\oplus$)	786^{+101}_{-82}	93^{+12}_{-10}	$43.2^{+5.6}_{-4.5}$
TSM [e]	41^{+36}_{-13}	123^{+231}_{-57}	90^{+71}_{-29}

[a] Maximum values reported as the 99 per cent upper credible limit.
[b] Derived using $g_p = GM_pR_p^{-2}$.
[c] Derived using sampled parameters following J. Southworth, P. J. Wheatley & G. Sams (2007).
[d] Assuming a zero albedo.
[e] Transmission spectroscopy metric (TSM) by E. M. R. Kempton et al. (2018).

measurement uncertainty. We did this 100 times to obtain 100 simulated activity-only RV and NGTS time-series, with similar noise properties and same time-sampling as the real data.

We first explore the question: could we have detected the planetary signals if there were no signals? We modelled each activity-only RV synthetic data set (i.e. with no planetary signals injected) using a three-planet and two-dimensional GP configuration as described in Section 3.4 with RV and NGTS-like model. For each simulation, we plot the posterior over the semi-amplitudes for the three 'planets' in the top column of Fig. 8, compared to the posterior obtained from the real data set. We then count the fraction of the simulations where we would have claimed 2σ detection for the three planets. For planet b, this occurred in 5 per cent of the times, for planet c in 1 per cent of the cases, and for planet d in 1 per cent of the cases. This suggests that 2σ estimates are unlikely to appear if the Doppler semi-amplitudes were zero. This is expected because we know a priori that TOI-451 b, c, and d exist, and we expect that there are Doppler signals larger than zero that is consistent with the ephemeris of the transiting signal.

We then repeat the same exercise, using the same 100 synthetic data sets, but this time, injecting three Keplerian signals with the median planet parameters reported in Table 4. Again, we modelled these synthetic data sets using `pyaneti` with the same configuration as described in Section 3.4. The resulting posteriors are shown in the bottom row of Fig. 8. First we ask the question, how often are TOI-451 b, c, and d detected at 2σ for a given confidence level from these simulations? We find that TOI-451 b, c, and d are detected 46 per cent, 15 per cent, and 43 per cent of the time, respectively. We then ask the question, what fraction of the time the injected semi-amplitudes are within 2σ of the recovered posterior distributions? We find that this happens on 96 per cent, 98 per cent, and 99 per cent of the times for TOI-451 b, c, and d, respectively. For Gaussian distributions we would expect this to be close to 95 per cent, making these results consistent with expectations. These injection tests suggest that the detected signals are unlikely to be entirely spurious. Nevertheless, our sensitivity to the planetary signatures appears to be significantly affected by stochastic stellar variability and instrumental white noise. Consequently, these results should be interpreted with caution.

4.2 Planets properties and mass-loss perspectives

In this section we explore the implications of the observed properties of the TOI-451 planets in the context of composition and atmospheric mass-loss. Tables 4 and 5 present the inferred planetary and orbital parameters that we will use to discuss the nature of the TOI-451 worlds. It is important to note that we did not detect any of the three transiting planets in the RVs with a significance $> 3\sigma$. We report the maximum Doppler semi-amplitudes and masses for the three planets in Tables 4 and 5. The masses of planets TOI-451 b and d are $M_b = 4.7^{+2.1}_{-2.2}$ $M_\oplus$ and $M_d = 10.2^{+4.6}_{-4.5}$ $M_\oplus$ (2σ confidence). TOI-451 c posterior distribution is less constrained and has a maximum mass of 11.5 $M_\oplus$. For this reason, we will only explore the possible properties for TOI-451 b and d. We will base our conclusions on the median values, but we are aware that the parameters credible intervals allow wider possibilities.

Fig. 9 shows mass-radius diagrams for small exoplanets ($1 < R_p < 5\,R_\oplus$ and $1 < M_p < 32\,M_\oplus$). Planets TOI-451 b and d are shown with relative composition models. TOI-451 c is shown with an arrow to indicate the 99 per cent upper credible limit. The plot also highlights other young exoplanets with reported masses and radii. The models assume planets with a Earth-like (1/3 iron and 2/3 silicates) and water-rich (50 per cent rocky and 50 per cent water) cores. We also show the hydrogen envelope mass fraction models for both core composition cases. To compute the solid core composition curves for rocky and water-rich planets, we adopted the theoretical mass–radius relations by L. Zeng, D. D. Sasselov & S. B. Jacobsen (2016) for an Earth-like rocky core and for a water-rich core. To compute the hydrogen composition curves for each planet, we assumed a two layer model with a gaseous envelope on top of a solid core. For the rocky core, we again adopted the models by L. Zeng et al. (2016) described above. For the gaseous envelope, we adopted the envelope struc-

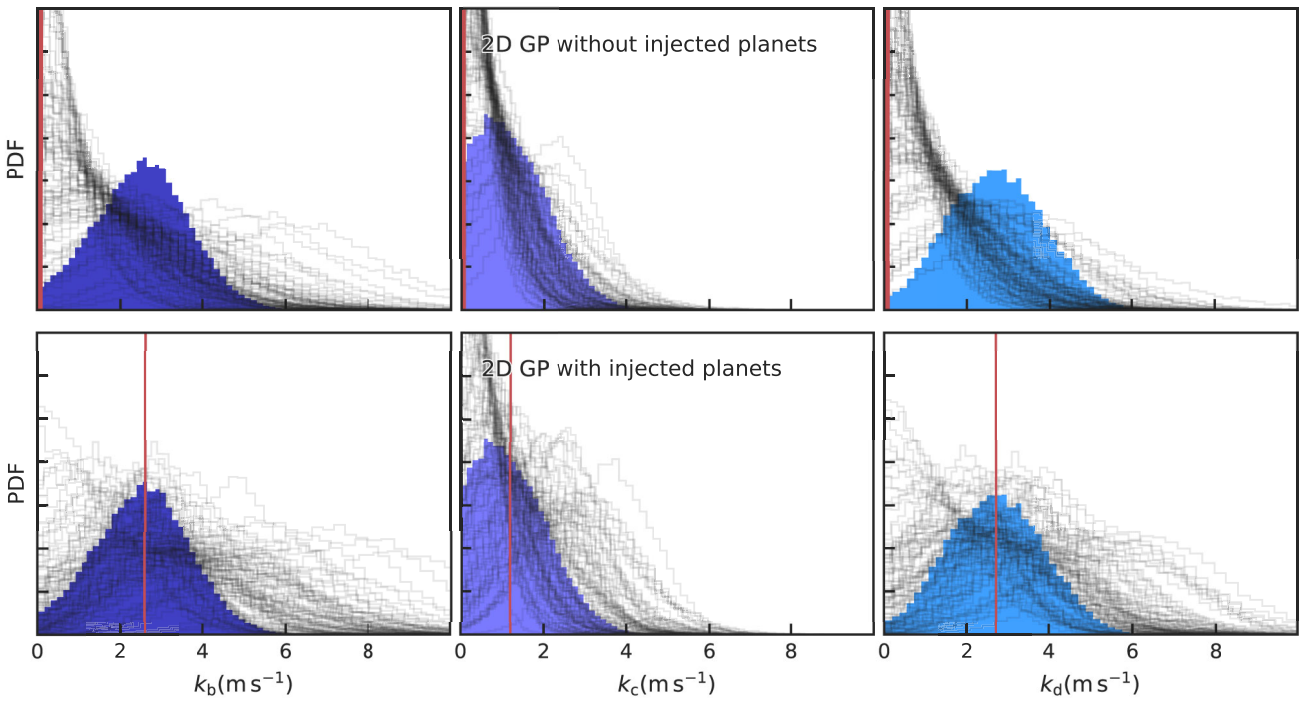

Figure 8. Results of the injection-recovery tests. The top panel shows the recovered posteriors for TOI-451 b, c, and d obtained from the activity-only time series. The bottom panel displays the posteriors derived from the time series that include both stellar activity and injected planetary signals, modelled with a 2D GP. In each panel, the filled histograms correspond to the posteriors from the original data set, while the thin grey lines represent the posteriors obtained from the simulated data sets. Vertical lines show the injected Doppler semi-amplitude for each case.

ture model by H. Chen & L. A. Rogers (2016), based on MESA simulations and for which they provide a polynomial fit valid for planet ages over 100 Myr and envelope mass fractions under 20 per cent.

The first thing to note from Fig. 9 is that there is an apparent dichotomy of young exoplanets that coincides with the radius gap (B. J. Fulton et al. 2017; V. Van Eylen et al. 2018). TOI-451 b is the only young exoplanet that lies within it, making it an excellent target to test mass-loss theories. If we assume that TOI-451 b has an Earth-like core surrounded by a hydrogen envelope, the planet would need an hydrogen envelope of 0.01 per cent of mass to explain its radius. Given the age of TOI-451, one would expect that the star has just past the peak of its magnetic activity and the most intense phase of photoevaporation could have already passed (J. E. Owen & Y. Wu 2017). However, atmospheric mass-loss could still be occurring by photoevaporation until roughly 1 Gyr (G. W. King & P. J. Wheatley 2021; J. G. Rogers & J. E. Owen 2021) and/or core-powered mass-loss (S. Ginzburg et al. 2016) at longer time-scales. This would make of TOI-451 b a planet that is on the verge of losing what remains of its atmosphere and move to the rocky side of the radius valley. The inferred characteristics of TOI-451 b suggest that the planet could still host a small hydrogen envelope. Therefore this planet is an excellent test to search for signatures of ongoing evaporation, for example by searching for escaping Helium in transmission spectroscopy (e.g. M. Zhang et al. 2022). However, TOI-451 b's nature could be different if we assume a different core composition. If TOI-451 b instead has a water-rich core, then the planet is consistent with being a solid world with no need of an envelope (see Fig. 9). This scenario would imply that photoevaporation has fully removed any initial envelope within the first 125 Myr.

Because of their radii, TOI-451 c and d are expected to be planets with a volatile-rich envelope rather than being solid (as suggested by previous works e.g. B. J. Fulton et al. 2017; V. Van Eylen et al. 2018). Depending on the assumed core composition for TOI-451 d, its radius can be explained by different fractions of hydrogen envelopes. Ranging from 8 per cent by mass for an Earth-like core, to 5 per cent by mass for a water rich core. Because of its youth, extended atmosphere, and host star brightness, TOI-451 d is an excellent candidate to perform transmission spectroscopy. We note that TOI-451 d has a Transmission spectroscopic metric (TSM) of 90^{+71}_{-29}, that is consistent with the threshold of 90 suggested by E. M. R. Kempton et al. (2018). This makes TOI-451 d a highly valuable target for the *JWST*. Furthermore, the mass provided in this work will be useful to interpret atmospheric observations (N. E. Batalha et al. 2019). We note that observations of TOI-451 c and d are scheduled to be observed with the *JWST* (GO 5959; A. Feinstein et al. 2024).

Fig. 10 shows the key-role of the TOI-451 system within the broader context of planetary evolution and atmospheric mass-loss processes. The current population of transiting planets displays a trend of decreasing radii with age that aligns well with the expected outcomes of the mass-loss mechanisms discussed in the previous paragraphs (see Panel b, Fig. 10). Within the photoevaporation framework, one would expect an evolutionary path in which planets become progressively denser as they lose a substantial fraction of their primordial envelopes during the first ∼100 Myr. Notably, the subset of well-characterized young exoplanets with ages younger than 100 Myr tends to exhibit lower bulk densities compared to those in the 100 Myr–1 Gyr range (see Panel c, Fig. 10). Although this pattern is still supported by a small number of systems, it provides valuable clues into atmo-

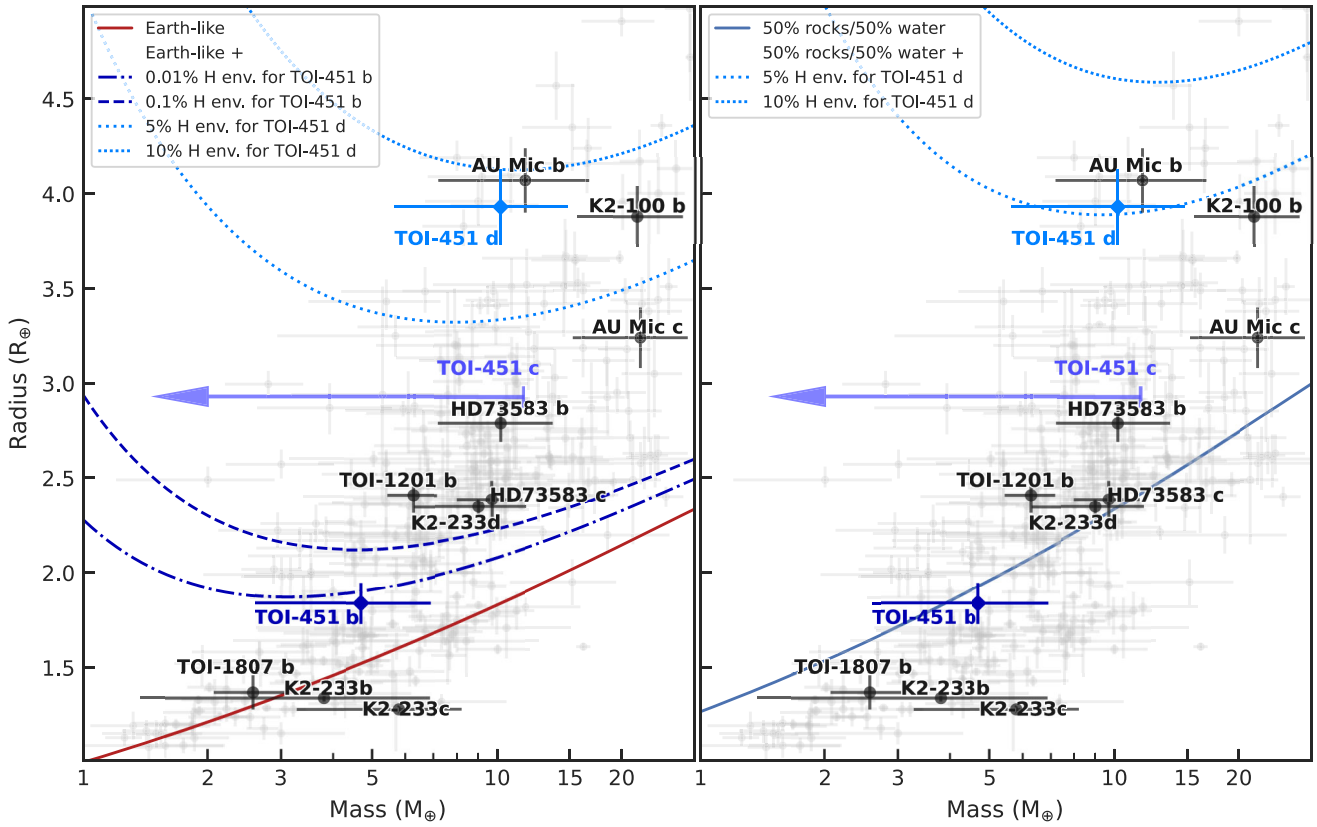

Figure 9. Mass *vs* radius diagram for small exoplanets ($1 < R_p < 5\,R_\oplus$ and $1 < M_p < 32\,M_\oplus$). Grey points with error bars show planets with mass and radius measurements better than 50 per cent (As in the NASA Exoplanet Archive on 2025 Dec 17, https://exoplanetarchive.ipac.caltech.edu/, J. L. Christiansen et al. 2025). Black points and labels refer to young exoplanets (<1 Gyr) with mass and radius measurements. TOI-451 b and d are shown with colourful diamonds and properly labelled. An arrow denotes the 99 per cent upper credible limit for TOI-451 c, illustrating the extent of possible values. Solid lines represent two-layer core models as given by L. Zeng et al. (2016). Non-solid lines correspond to cores surrounded by a hydrogen envelope properly labelled in each inset. This plot was created using the same code used to create the mass-radius diagram in O. Barragán et al. (2018).

spheric evolution. Additional well-characterized young planets are required to confirm whether this constitutes a robust evolutionary trend. The TOI-451 system, with its precisely determined age and multiple transiting planets, emerges as a cornerstone laboratory for testing photoevaporation efficiency. In particular, TOI-451 b may represent a planet that has just passed through an intense stage of high-energy irradiation. The inferred density values derived here will therefore serve as a key reference for future follow-up observations and modelling efforts. Nonetheless, improved mass constraints will be crucial to refine the present interpretation.

4.3 On follow-up observations

TOI-451 is a keystone target that can help to understand the evolution of multiplanetary systems, but additional follow-up observations are needed to improve the precision of the planetary and orbital parameters. In particular, additional RV monitoring to refine the planet masses is needed. The results presented in this paper suggest that TOI-451 b could still retain a small fraction of primordial atmosphere, or being a water world. Both scenarios are interesting for testing planetary evolution and mass-loss theories. Improvement of masses for TOI-451 c and d are also essential. Being young worlds with significant atmospheric envelopes, they are excellent candidates to perform transmission spectroscopy studies. But the interpretations of such are only useful if masses are known (N. E. Batalha et al. 2019).

How many more RV measurements would we need to improve the mass measurements of TOI-451 b, c and d? To answer this question, we used `citlalatonac` (O. Barragán et al. 2022a) to simulate multiple realizations of additional ESPRESSO observations and analysed them in the same way as we analysed the existing data in this paper. We used the GP hyper-parameters obtained in Table 4 to create the stellar signal as samples of a multi-GP. We simulated synthetic time-series of activity-induced RV and NGTS-like photometry and added the expected Keplerian signals for the three planets and sampled the data assuming TOI-451 is observed from Paranal with a maximum airmass of 1.7 in an intensive five months campaign, and added realistic white and instrumental red noise (based on our existing ESPRESSO data). We then attempted to recover the stellar and planetary signals, using the same multi-GP framework and combining the existing and simulated data, as we have done with the available real data. By varying the number of synthetic observations, we established that we need around 125 more epochs spread over five months to model the stellar signal robustly and to detect the signal of planets to 3σ confidence or better.

By the end of 2026 ESA's upcoming M-Class mission, *PLATO* (H. Rauer et al. 2024) is planned to be launched. *PLATO* is observing a fixed field in the Southern hemisphere (V. Nascimbeni et al.

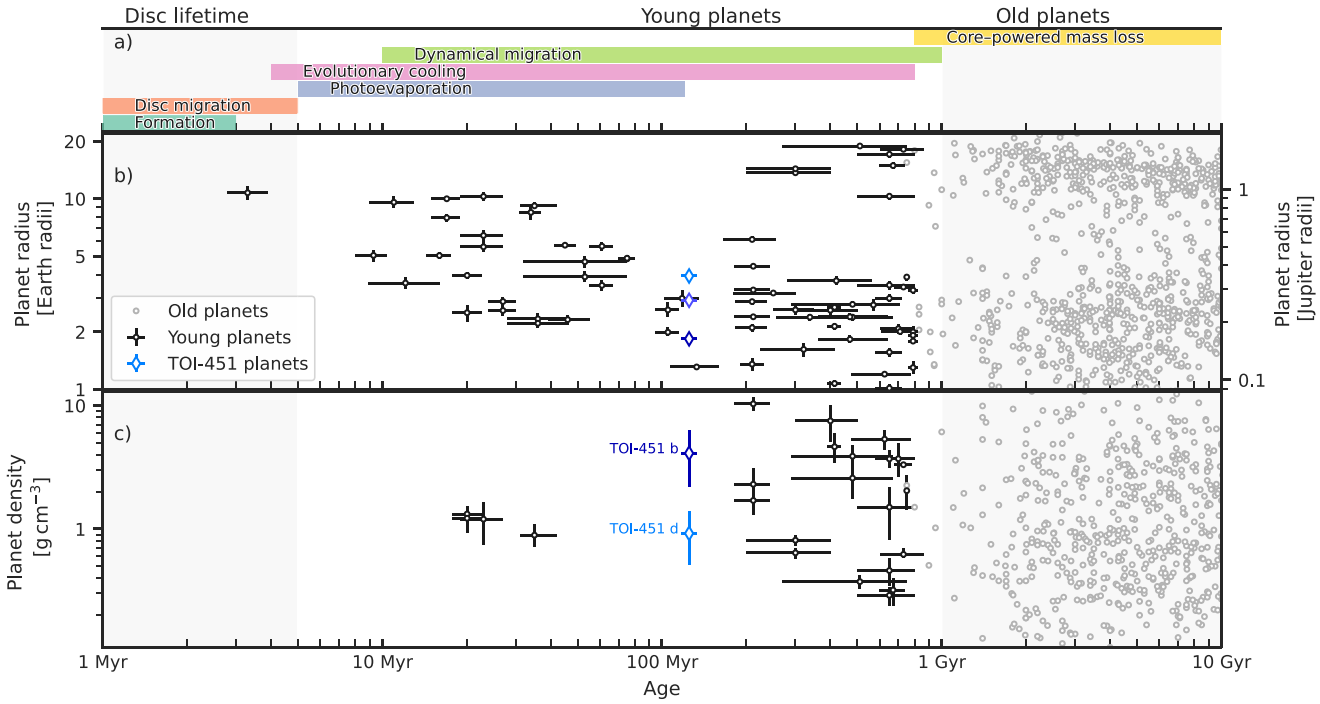

Figure 10. (a) Time-scales of key planetary evolutionary processes. (b) Planetary radius and (c) planetary density as functions of system age. Old exoplanets are shown as grey dots, and known young exoplanets are indicated by dark dots (As in the NASA Exoplanet Archive on 2025 Dec 17, https://exoplanetarchive.ipac.caltech.edu/, J. L. Christiansen et al. 2025). Our radius and density estimates for TOI-451 b, c, and d are shown with diamonds.

2025) for at least the first two years of its mission. The spacecraft has 26 cameras that partially overlap resulting in stars within the field being observed by up to 24 cameras in the centre and down to 6 at the edges. TOI-451 lies within the Southern *PLATO* field (Y. N. E. Eschen et al. 2024) and is a target of the *PLATO* Input Catalogue (PIC; M. Montalto et al. 2021). Currently it is estimated that *PLATO* shall observe this target with 6 cameras for at least the first two years of its mission. Due to *PLATO* observing the target with more cameras than *TESS* and for a longer duration, it improves the sensitivity to detecting smaller and long-orbital period planets. For TOI-451 the estimated noise recorded in the PIC, results in sensitivities allowing to detect planets as small as 0.5 $R_\oplus$ and planets at orbital periods of up to 200 d if they transit this star (Y. N. E. Eschen et al. 2024).

5 CONCLUSIONS

In this study, we performed an intensive photometric and spectroscopic ground-based follow-up of TOI-451 to further characterise the properties of the TOI-451 planetary system. Our analysis provides 2σ masses estimates for TOI-451 b and d that allowed us to infer, at first order, their possible nature, as well as a upper mass limit for TOI-451 c.

Our analysis highlights TOI-451 b as uniquely positioned within the radius gap, making it a crucial target for testing atmospheric mass-loss theories. If composed primarily of an Earth-like rocky core, TOI-451 b would retain a minimal hydrogen envelope, potentially indicating ongoing atmospheric-loss processes. Conversely, if TOI-451 b has a rocky-ice composition, its radius can be explained without the need of an atmospheric envelope, suggesting efficient mass-loss within the first 125 Myr. Planet TOI-451 d is likely enveloped by a substantial volatile-rich atmosphere. Depending on its core composition, hydrogen envelopes between 5 per cent and 8 per cent by mass could explain its observed radius. Its youth, substantial atmosphere, and brightness of its host star position TOI-451 d as an optimal candidate for transmission spectroscopy. Planned *JWST* observations of TOI-451 c and d will further refine our understanding, leveraging the mass constraints provided by this study to better interpret atmospheric characterization results.

This manuscript was also a proof-of-concept on the use of contemporaneous spectroscopic-photometry observations within the context of multi-GP regression. We showed the potential of using contemporaneous photometry as an activity indicator. However, we note that our photometric sampling strategy was similar to the spectroscopic one, of taking one point per night. It is still to be tested the usefulness of having continuous and high precision contemporaneous photometry, e.g. space photometry, when modelling stellar signals in RVs. We foresee that contemporaneous and high-cadence photometry will be useful in cases where the stellar activity evolves faster or similar to the time-scales in which the spectroscopic observations are taken (e.g. young stars). This scenario has to be explore further given the upcoming *PLATO* mission that will provide high-quality continuos photometry that could be paired with contemporaneous RV follow-ups. The *PLATO* observing strategy combined with its 24-camera strategy will deliver high-quality light curves with high signal-to-noise astrophysical signals (e.g. O. Barragán, S. Aigrain & J. McCormac 2024a).

ACKNOWLEDGEMENTS

Based on observations collected at the European Organisation for Astronomical Research in the Southern Hemisphere un-

der ESO programmes 0112.C-0347(A) and 0112.C-0131(A). This work is based in part on data collected under the NGTS project at the ESO La Silla Paranal Observatory. The NGTS facility is operated by a consortium of institutes with support from the UK Science and Technology Facilities Council (STFC) under projects ST/M001962/1, ST/S002642/1, and ST/W003163/1. This work makes use of observations from the Las Cumbres Observatory global telescope network. This publication made use of data products from the Wide-field Infrared Survey Explorer, which is a joint project of the University of California, Los Angeles, and the Jet Propulsion Laboratory/California Institute of Technology, funded by the National Aeronautics and Space Administration. This research has made use of the NASA Exoplanet Archive, which is operated by the California Institute of Technology, under contract with the National Aeronautics and Space Administration under the Exoplanet Exploration Program. We thank the anonymous referees for their careful reading of the manuscript and comments that helped to improve the quality of the work. OB, HY, BK, and SA acknowledge that this publication is part of a project that has received funding from the European Research Council (ERC) under the European Union's Horizon 2020 research and innovation programme (grant agreement no. 865624). MM, VB, and NL acknowledge financial support from the Agencia Estatal de Investigación (AEI/10.13039/501100011033) of the Ministerio de Ciencia e Innovación through project PID2022-137241NB-C41, AVF acknowledges the support of the IOP through the Bell Burnell Graduate Scholarship Fund. AM acknowledges funding from a UKRI Future Leader Fellowship, grant number MR/X033244/1 and a UK Science and Technology Facilities Council (STFC) small grant ST/Y002334/1. SS acknowledges Fondo Comité Mixto-ESO Chile ORP 025/2022. YNEE acknowledges support from a Science and Technology Facilities Council (STFC) studentship, grant number ST/Y509693/1. EMV acknowledges financial support from the Swiss National Science Foundation (SNSF) Postdoc. Mobility Fellowship under grant no. P500PT_225456/1. ML acknowledged that this research was in part funded by the UKRI (Grant EP/X027562/1). FM acknowledges the financial support from the Agencia Estatal de Investigación del Ministerio de Ciencia, Innovación y Universidades (MCIU/AEI) through grant PID2023-152906NA-I00. JSJ gratefully acknowledges support by FONDECYT grant 1240738 and from the ANID BASAL project FB210003. This work made use of NUMPY (C. R. Harris et al. 2020), MATPLOTLIB (J. D. Hunter 2007), and PANDAS (The pandas development team 2020) libraries. This work made use of ASTROPY:[6] a community-developed core PYTHON package and an ecosystem of tools and resources for astronomy (Astropy Collaboration 2013, 2018, 2022). OB, HY, BK, EMV, MC, and SA acknowledge that they miss that fusion restaurant that provided the calories to write this paper.

DATA AVAILABILITY

The codes used in this manuscript are freely available at https://github.com/oscaribv. The spectroscopic measurements that appear in Table 2 are available as supplementary material in the online version of this manuscript. All *TESS* data are available via the MAST archive.

[6] http://www.astropy.org

REFERENCES

Ahrer E.-M. et al., 2023, Nature, 614, 653
Aigrain S., Pont F., Zucker S., 2012, MNRAS, 419, 3147
Allard F., Homeier D., Freytag B., 2012, Phil. Trans. R. Soc. A, 370, 2765
Astropy Collaboration, 2013, A&A, 558, A33
Astropy Collaboration, 2018, AJ, 156, 123
Astropy Collaboration, 2022, ApJ, 935, 167
Barragán O. et al., 2018, A&A, 612, A95
Barragán O., Gandolfi D., Antoniciello G., 2019a, MNRAS, 482, 1017
Barragán O. et al., 2019b, MNRAS, 490, 698
Barragán O., Aigrain S., Gillen E., Gutiérrez-Canales F., 2021, Res. Notes AAS, 5, 51
Barragán O., Aigrain S., Rajpaul V. M., Zicher N., 2022a, MNRAS, 509, 866
Barragán O. et al., 2022b, MNRAS, 514, 1606
Barragán O. et al., 2023, MNRAS, 522, 3458
Barragán O., Aigrain S., McCormac J., 2024a, RAS Techn. Instr., 3, 198
Barragán O. et al., 2024b, MNRAS, 531, 4275
Batalha N. E., Lewis T., Fortney J. J., Batalha N. M., Kempton E., Lewis N. K., Line M. R., 2019, ApJ, 885, L25
Beard C. et al., 2025, AJ, 169, 92
Blanco-Cuaresma S., 2019, MNRAS, 486, 2075
Blunt S. et al., 2023, AJ, 166, 62
Bressan A., Marigo P., Girardi L., Salasnich B., Dal Cero C., Rubele S., Nanni A., 2012, MNRAS, 427, 127
Brown T. M. et al., 2013, PASP, 125, 1031
Bryant E. M. et al., 2020, MNRAS, 494, 5872
Castelli F., Kurucz R. L., 2004, preprint (astro-ph/0405087)
Chen H., Rogers L. A., 2016, ApJ, 831, 180
Choi J., Dotter A., Conroy C., Cantiello M., Paxton B., Johnson B. D., 2016, ApJ, 823, 102
Christiansen J. L. et al., 2025, Planet. Sci. J., 6, 186
Collins K. A., Kielkopf J. F., Stassun K. G., Hessman F. V., 2017, AJ, 153, 77
Cretignier M., 2022, PhD thesis, Univ. Geneva, Switzerland
Cretignier M., Dumusque X., Allart R., Pepe F., Lovis C., 2020a, A&A, 633, A76
Cretignier M., Francfort J., Dumusque X., Allart R., Pepe F., 2020b, A&A, 640, A42
Cretignier M., Dumusque X., Aigrain S., Pepe F., 2023, A&A, 678, A2
Cretignier M. et al., 2024, MNRAS, 535, 2562
Cutri R. M. et al., 2003, VizieR Online Data Catalog. p. II/246
Dalal S. et al., 2024, MNRAS, 531, 4464
Eschen Y. N. E., Bayliss D., Wilson T. G., Kunimoto M., Pelisoli I., Rodel T., 2024, MNRAS, 535, 1778
Feinstein A. et al., 2024, KRONOS: Keys to Revealing the Origin and Nature Of sub-neptune Systems, JWST Proposal. Cycle 3, ID. #5959.
Foreman-Mackey D., Hogg D. W., Lang D., Goodman J., 2013, PASP, 125, 306
Freckelton A. V. et al., 2024, MNRAS, 531, 4085
Fridlund M. et al., 2024, A&A, 684, A12
Fulton B. J. et al., 2017, AJ, 154, 109
Gaia Collaboration, 2020, VizieR Online Data Catalog. p. I/350
Gandolfi D. et al., 2018, A&A, 619, L10
Gelman A., Rubin D. B., 1992, Stat. Sci., 7, 457
Ginzburg S., Schlichting H. E., Sari R., 2016, ApJ, 825, 29
González Hernández J. I. et al., 2024, A&A, 690, A79
Gray R. O., Corbally C. J., 1994, AJ, 107, 742
Gregory P. C., 2005, ApJ, 631, 1198
Harris C. R. et al., 2020, Nature, 585, 357
Haywood R. D. et al., 2014, MNRAS, 443, 2517
Høg E. et al., 2000, A&A, 355, L27
Huerta M., Johns-Krull C. M., Prato L., Hartigan P., Jaffe D. T., 2008, ApJ, 678, 472
Hunter J. D., 2007, Comput. Sci. Eng., 9, 90
Husser T. O., Wende-von Berg S., Dreizler S., Homeier D., Reiners A., Barman T., Hauschildt P. H., 2013, A&A, 553, A6

Kempton E. M. R. et al., 2018, PASP, 130, 114401
King G. W., Wheatley P. J., 2021, MNRAS, 501, L28
Kipping D. M., 2013, MNRAS, 435, 2152
Klein B. et al., 2024, MNRAS, 531, 4238
Kokori A. et al., 2023, ApJS, 265, 4
Kurucz R. L., 1993, SYNTHE Spectrum Synthesis Programs and Line Data. Kurucz CD-ROM
Kurucz R. L., 2005, Mem. Soc. Astron. Ital. Suppl., 8, 14
Lanza A. F., 2006, MNRAS, 373, 819
Luque R. et al., 2023, Nature, 623, 932
Mandel K., Agol E., 2002, ApJ, 580, L171
Mayo A. W. et al., 2019, AJ, 158, 165
McCully C., Volgenau N. H., Harbeck D.-R., Lister T. A., Saunders E. S., Turner M. L., Siiverd R. J., Bowman M., 2018, in Guzman J. C., Ibsen J., eds, Proc. SPIE Conf. Ser. Vol. 10707, Software and Cyberinfrastructure for Astronomy V. SPIE, Bellingham, p. 107070K
Montalto M. et al., 2021, A&A, 653, A98
Morris B. M., 2020, ApJ, 893, 67
Morton T. D., 2015, Astrophysics Source Code Library, record ascl:1503.010
Nardiello D. et al., 2022, A&A, 664, A163
Nari N. et al., 2025, A&A, 693, A297
Nascimbeni V. et al., 2025, A&A, 694, A313
Newton E. R. et al., 2021, AJ, 161, 65
Nicholson B. A., Aigrain S., 2022, MNRAS, 515, 5251
O'Brien S. M. et al., 2022, MNRAS, 509, 6111
Owen J. E., Wu Y., 2013, ApJ, 775, 105
Owen J. E., Wu Y., 2017, ApJ, 847, 29
Pepe F. et al., 2021, A&A, 645, A96
Queloz D. et al., 2001, A&A, 379, 279
Rajpaul V., Aigrain S., Osborne M. A., Reece S., Roberts S., 2015, MNRAS, 452, 2269
Rajpaul V., Aigrain S., Roberts S., 2016, MNRAS, 456, L6
Rajpaul V. M., Barragán O., Zicher N., 2024, MNRAS, 530, 4665
Rauer H. et al., 2025, Experimental Astronomy, 59, 26
Ricker G. R. et al., 2015, J. Astron. Telesc. Instrum. Syst., 1, 014003
Rogers J. G., Owen J. E., 2021, MNRAS, 503, 1526
Saar S. H., Donahue R. A., 1997, ApJ, 485, 319
Southworth J., Wheatley P. J., Sams G., 2007, MNRAS, 379, L11
Speagle J. S., 2020, MNRAS, 493, 3132
Stalport M. et al., 2023, A&A, 678, A90
Stassun K. G. et al., 2019, AJ, 158, 138
Suárez Mascareño A. et al., 2021, Nat. Astron., 6, 232
Suárez Mascareño A. et al., 2023, A&A, 670, A5
The pandas development team, 2020, pandas-dev/pandas: Pandas, Zenodo, Version v3.0.0rc2
Van Eylen V., Agentoft C., Lundkvist M. S., Kjeldsen H., Owen J. E., Fulton B. J., Petigura E., Snellen I., 2018, MNRAS, 479, 4786
Vines J. I., Jenkins J. S., 2022, MNRAS, 513, 2719
Wheatley P. J. et al., 2018, MNRAS, 475, 4476
Winn J. N., 2010, preprint (arXiv:1001.2010)
Yu H. et al., 2025, MNRAS, 536, 2046
Zechmeister M., Kürster M., 2009, A&A, 496, 577
Zechmeister M. et al., 2018, A&A, 609, A12
Zeng L., Sasselov D. D., Jacobsen S. B., 2016, ApJ, 819, 127
Zhang M., Knutson H. A., Wang L., Dai F., Barragán O., 2022, AJ, 163, 67
Zicher N. et al., 2022, MNRAS, 512, 3060

SUPPORTING INFORMATION

Supplementary data are available at *MNRAS* online.

table2

Please note: Oxford University Press is not responsible for the content or functionality of any supporting materials supplied by the authors. Any queries (other than missing material) should be directed to the corresponding author for the article.

[1]*Sub-department of Astrophysics, Department of Physics, University of Oxford, Oxford OX1 3RH, UK*
[2]*Department of Physics, University of Warwick, Coventry CV4 7AL, UK*
[3]*Instituto de Astrofisica de Canarias (IAC), Calle Vía Láctea s/n, E-38205 La Laguna, Tenerife, Spain*
[4]*Departamento de Astrofísica, Universidad de La Laguna (ULL), E-38206 La Laguna, Tenerife, Spain*
[5]*Centre for Exoplanets and Habitability, University of Warwick, Gibbet Hill Road, Coventry CV4 7AL, UK*
[6]*School of Physics and Astronomy, University of Birmingham, Edgbaston, Birmingham B15 2TT, UK*
[7]*Instituto de Astronomía, Universidad Católica del Norte, Angamos 0610, 1270709 Antofagasta, Chile*
[8]*Astronomy Unit, Queen Mary University of London, G.O. Jones Building, Bethnal Green, London E1 4NS, UK*
[9]*Observatoire de Genève, Université de Genève, Chemin Pegasi, 51, CH-1290 Versoix, Switzerland*
[10]*SUPA School of Physics and Astronomy, University of St Andrews, North Haugh, St Andrews KY16 9SS, UK*
[11]*Instituto de Estudios Astrofísicos, Facultad de Ingeniería y Ciencias, Universidad Diego Portales, Av. Ejército Libertador 441, 8370191 Santiago, Chile*
[12]*Centro de Excelencia en Astrofísica y Tecnologías Afines (CATA), Camino El Observatorio 1515, Las Condes, 7591245 Santiago, Chile*
[13]*Center for Astrophysics, Harvard & Smithsonian, 60 Garden St, Cambridge, MA 02138, USA*
[14]*Faculty of Physics, University Observatory, Ludwig-Maximilians-Universität München, Scheinerstr. 1, D-81679 Munich, Germany*

This paper has been typeset from a TEX/LATEX file prepared by the author.